

Effects of Varying Alx Moles on the Structure and Luminescence Properties of $ZnAl_xO_{1.5x} + 1:0.1\%$ Tb³⁺ Nano Phosphor Prepared using Citrate sol-gel Method

V Maphiri

Sefako Makgatho Health Sciences University

L Melato

Vaal University of Technology

MR Mhlongo

Sefako Makgatho Health Sciences University

TT Hlatshwayo

University of Pretoria

TE Motaung

University of South Africa

LF Koao

University of the Free State - Qwaqwa Campus

Setumo Victor Motloung (✉ cchataa@gmail.com)

Nelson Mandela University <https://orcid.org/0000-0002-4085-3927>

Research Article

Keywords: Citrate sol-gel, Spinel, Tb³⁺-doped, Alx moles, CIE

Posted Date: March 23rd, 2021

DOI: <https://doi.org/10.21203/rs.3.rs-348042/v1>

License:  This work is licensed under a Creative Commons Attribution 4.0 International License.

[Read Full License](#)

Effects of varying Al_x moles on the structure and luminescence properties of $ZnAl_xO_{1.5x+1}:0.1\%$

Tb^{3+} nano phosphor prepared using citrate sol-gel method

V.M. Maphiri^{1*}, L.T. Melato², M.R. Mhlongo¹, T.T. Hlatshwayo³, T.E. Motaung^{4,5}, L.F. Koao⁶,

S.V. Motloun^{1,7}**

¹Department of Physics, Sefako Makgatho Health Science University, P. O. Box 94, Medunsa, 0204,
South Africa

²Department of Physics and Non Destructive Testing, Vaal University of Technology, Andries
Potgieter Blvd, Vanderbijlpark, 1900, South Africa

³Department of Physics, University of Pretoria, Pretoria, 0002, South Africa

⁴Department of Chemistry, School of Science in the College of Science Engineering and Technology,
University of South Africa, Preller Street, Muckleneuk Ridge, City of Tshwane, PO Box 392, UNISA
0003, South Africa

⁵Department of Chemistry, Sefako Makgatho Health Science University, P. O. Box 94, Medunsa,
0204, South Africa

⁶Department of Physics, University of the Free State (Qwaqwa Campus), Private Bag X13,
Phuthaditjhaba 9866, South Africa

⁷Department of Physics, Nelson Mandela University, P. O. Box 77000, Port Elizabeth 6031, South
Africa

Corresponding author:

E-mail: Vusanimuswamaphiri@gmail.com and cchataa@gmail.com (S.V. Motloun)

Abstract. Un-doped and $ZnAl_xO_{(1.5x+1)}:0.1\%$ Tb^{3+} (ZAOT) nano-powders were synthesized via citrate sol-gel method. The Al_x moles were varied in the range of $0.25 \leq x \leq 5.0$. The X-ray powder diffraction (XRD) data revealed that for the $x < 1.5$, the prepared samples crystal structure consists of mixed phases of the cubic $ZnAl_2O_4$ and hexagonal ZnO phases, while for the $x \geq 1.5$ the structure consists of single

phase of cubic ZnAl_2O_4 . This was confirmed by the Raman and Fourier-Transform Infrared (FTIR) vibrational spectroscopy. Scanning electron microscopy (SEM) showed that varying Al_x moles influences the morphology while Transmission electron microscopy (TEM) shows the dual morphology at $x < 1.5$. The photoluminescence (PL) revealed intense and distinct emissions attributed to both the host and Tb^{3+} transitions. The emission intensity highly depends on the Al_x moles. The International Commission on Illumination (CIE) colour chromaticity showed that the emission colour could be tuned by varying the Al_x moles.

Keywords: Citrate sol-gel; Spinel; Tb^{3+} -doped; Al_x moles; CIE

1. Introduction

In the past few decades, metal oxides (MO) have enticed many researches in different field due to their unique physical and chemical properties [1]. MO are on the cutting edge of technology in various field of science such as water splitting [2–4], energy storage and conversions [5,6], photoluminescence (PL) [7–9] and transparent conducting oxide [1,10,11]. This is because of their band gap located directly at the Γ point which was determined theoretically and experimentally to be around few electron volts (eV) [12–14]. The MO denoted by the AB_2O_4 formula are usually referred to as spinel family group, which contains around 120 compound members with ZnAl_2O_4 (known as zinc aluminate or gahnite) being one of the prominent species in the PL field [1,15]. The ZnAl_2O_4 normally crystallizes in the cubic crystal structures of the $Fd\bar{3}m$ space group, where Zn and Al respectively occupies the tetrahedral (T_d) and octahedral (O_h) sites in the crystal matrix while oxygen atoms occupies the Wyckoff 32e position located at (u, u, u) , where $u \approx 0.25$ [1,16,17]. The positioning of the atoms or the structural configuration of the ZnAl_2O_4 depends on synthesis parameter such as the temperature [18,19] or concentration of the constituent elements [9,15,20]. These can lead in the crystallisation of metal ion in the normal (ZnAl_2O_4) configuration as described above (where Zn occupies T_d and Al occupies O_h sites) or in an inversion ($\text{Al}[\text{ZnAl}]_2\text{O}_4$) configuration where the T_d is now fully occupied by Al ion and the O_h

sites is half-sheared by Al and Zn ions. The spinel can also crystallise in between the normal and inversion configurations where ions occupy those sites spatial. Raman spectroscopy has been an wonderful technique of detecting such behaviours [17,20,21].

Various studies have been conducted on ZnAl_2O_4 in order to optimize and tune the emission colour. Most researchers introduce foreign ions (i.e. dopants) mostly from the lanthanides or rare earths within the different host at various doping concentrations [7–9,22–24]. Trivalent terbium ion (Tb^{3+}) is one of the most explored dopant due to its emission broadband covering the entire visible wavelength with an intense green emission colour around 525-560 nm [19,22–25]. Tb^{3+} has been triply [22,26], co-doped [23,24] with other dopants and singly doped [18,27] into ZnAl_2O_4 with the main aim of luminescence intensity optimization, colour tuning [28] and/or increasing emission life time [28,29]. The previous reports [18,19,22–24] on Tb^{3+} -doped studies showed a successful incorporation of dopants within the ZnAl_2O_4 matrix which led to some astonishing results, some of the results are; the possibility of a full-colour field emission from the doped ZnAl_2O_4 and the presence of two energy transfer (ET) system. The intra-ET within Tb^{3+} ions and between Tb^{3+} to Mn^{2+} , which were described as follows $\text{Tb}^{3+} (^5\text{D}_3) + \text{Tb}^{3+} (^7\text{F}_6) \rightarrow \text{Tb}^{3+} (^5\text{D}_4) + \text{Tb}^{3+} (^7\text{F}_{2,1,0})$ and $\text{Tb}^{3+} \rightarrow \text{Mn}^{2+}$ [23], respectively. The intra-ET happened via overlapping of the Tb^{3+} band and ET between Tb and Mn happened via the absorption of excitation energy at 350 nm from Tb^{3+} by the 654 nm emission peak of Mn^{2+} transitions. Most of the reported work on ZnAl_2O_4 focuses on the dopants and synthesis conditions. The effects of the metal ions (i.e. Zn and Al) moles in $\text{ZnAl}_2\text{O}_4:0.1\% \text{Tb}^{3+}$ has not been investigated in detail as far as the structural and optical properties are concern. Few studies were reported in the field such as that of catalysis [30,31]. The influence of the Mg_x moles was investigated on the $\text{Mg}_x\text{Al}_2\text{O}_{3+x}: 0.88\% \text{Cd}^{2+}$ system. The XRD and PL results showed a change in the structural phases and the dependence of photoluminescence on the Mg_x moles, respectively.

The effect of Al_x mole on the structure and luminescence properties of $\text{ZnAl}_x\text{O}_{1.5x+1}:0.1\% \text{Tb}^{3+}$ (ZAOT) has not been reported in literature to date. Thus, this investigation explores the influence of varying the Al_x moles ($0.25 \leq x \leq 5.0$) on the structure, morphology and PL properties of ZAOT system, with the main aim of producing alternative phosphor material for the practical application of lighting technology

such as light emitting diodes (LEDs). The observed PL emission channels are proposed and explained in details.

2. Experimental

2.1. Synthesis

The $\text{ZnAl}_x\text{O}_{1.5x+1}:0.1\% \text{Tb}^{3+}$ ($0.25 \leq x \leq 5.0$) series was synthesized via citrate sol-gel technique. The materials were prepared by dissolving stoichiometric masses of zinc nitrates hexa-hydrate [$\text{Zn}(\text{NO}_3)_2 \cdot 6\text{H}_2\text{O}$, 99.9%] corresponding to 1 mol while aluminium nitrates nano-hydrate [$\text{Al}(\text{NO}_3)_3 \cdot 9\text{H}_2\text{O}$, 98.5%] was added at the range of $0.25 \leq x \leq 5.0$ mol; citric acid (CA) [$\text{C}_6\text{H}_8\text{O}_7 \cdot \text{H}_2\text{O}$, 99%] was also dissolved in deionized water to chelate and stabilize the solution [32,33]. The stoichiometric molar ratios of Zn:CA was kept constant at 1:0.75 for all the prepared powder samples while varying the moles of Al^{3+} . A specified amount of terbium nitrate penta-hydrate [$\text{Tb}(\text{NO}_3)_3 \cdot 5\text{H}_2\text{O}$, 99.9%] was added to dope with 0.1% Tb^{3+} . The solution was heated at $\sim 80^\circ\text{C}$ while constantly stirring using the magnetic stirrer until the gels were formed. The gels were dried for 12 hour (h) in room temperature and subsequently annealed at 1000°C in a furnace for 1 h. The resulting solid-like-foam products were ground into fine powder samples using the pestle and mortar.

2.2. Characterization

The powder samples were analyzed with the Bruker D8-Advance powder X-ray powder diffraction (XRD) with a $\text{CuK}\alpha$ (1.5405 \AA) radiation, Witec alpha 300 RAS+ (Raman spectroscopy) using the 532 nm at 2 mW and Bruker Alpha platinum-ATR Fourier-transform infrared spectroscopy (FTIR) in the range of 400 to 1000 cm^{-1} was used to analyze the crystal structure, phase, functional group and the vibration bands. The structural phase from the XRD were identified using X'pert Highscore plus software and the relative phase quantification (%) were estimated using the Rietveld method. The particle shape, surface morphology and elementary constituents were characterized by the Zeiss Supra

55 scanning electron microscope (SEM) at 20 kV coupled with an energy dispersive X-ray spectroscopy (EDS). Crystallite shape and sizes was analysed via the JEOL JEM 1010 transmission electron microscopy (TEM). The room temperature (RT) photoluminescence (PL) spectra and lifetime measurements were performed by the Hitachi F-7000 fluorescence spectrophotometer using a 150 W monochromatized Xenon lamp as an excitation source.

3. Results and discussion

3.1. X-ray powder diffraction

The XRD patterns of the prepared samples are shown in Fig. 1. The diffraction peaks of these polycrystalline could be indexed to the standard patterns of the hexagonal ZnO (JCPDS 80-80075 and space group P63mc No. 186) and cubic ZnAl₂O₄ (JCPDS 82-1043 and space group Fd $\bar{3}$ m No. 227). The quantification percentages of these phases are shown on Table 1. The results show that the ZnO phase decreased with an increase in Al_x moles up to x = 1.0. ZnAl₂O₄ phase increased with an increase in Al_x moles. The unit cell of the ZnO and ZnAl₂O₄ were created using VESTA software (Ver. 3.5.2, 64-bit Edition) and crystallographic information files corresponding to the P63mc No. 186 and Fd $\bar{3}$ m No. 227 space group, respectively and the generated images are displayed on Fig. 2. From Fig. 1, it can be seen that at a lower Al_x moles of x < 1.5, the XRD patterns consists of the mixed phases of both the hexagonal ZnO and cubic ZnAl₂O₄. This observation is attributed to the insufficient Al atoms to bond with the Zn atoms to completely form ZnAl₂O₄. This led to the excess Zn²⁺ which amalgamated with O²⁻ to form ZnO. Similar XRD with both ZnO/ZnAl₂O₄ has been reported in Ref [17,25]. When x ≥ 1.5 the results suggest that the samples constitute of only cubic ZnAl₂O₄ phase, which is attributed to enough Al atoms available to completely form ZnAl₂O₄. This results suggest that the transition from dual ZnAl₂O₄/ZnO mixed phases to ZnAl₂O₄ single phase is somewhere around x = 1.5. Thus, the mixed phase/s in ZAOT highly depends on the Al_x moles. The XRD patterns of the doped (x = 2.0) and undoped (x = 2.0*) are similar, signifying a successful incorporation of Tb³⁺ within the ZnAl₂O₄ crystal lattice.

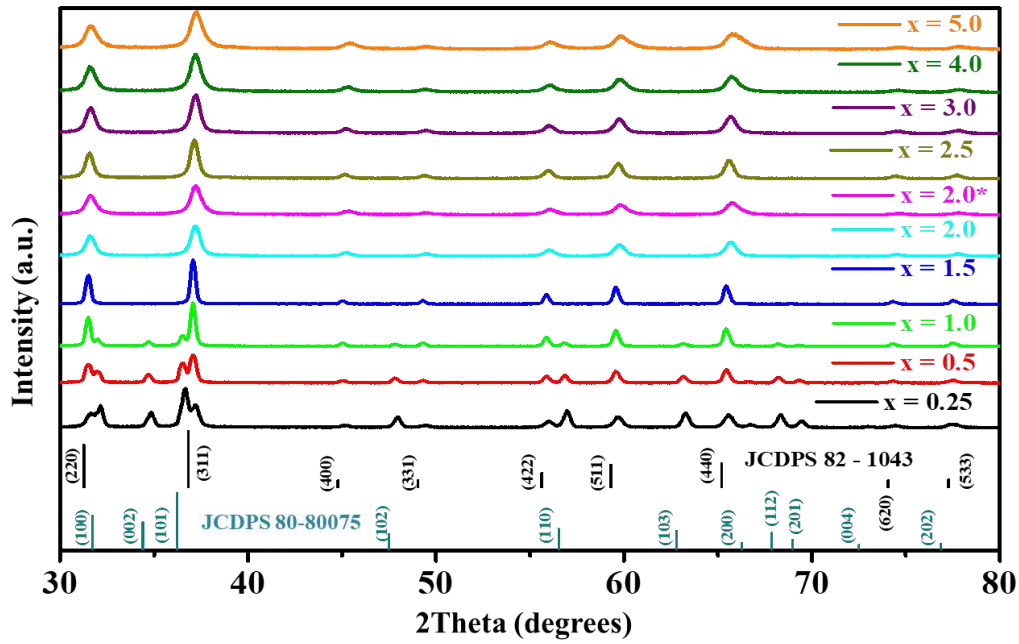


Fig. 1 The XRD pattern for the $x = 2.0^*$ (un-doped) and $\text{ZnAl}_x\text{O}_{1.5x+1}:0.1\% \text{Tb}^{3+}$ ($0.25 \leq x \leq 5.0$)

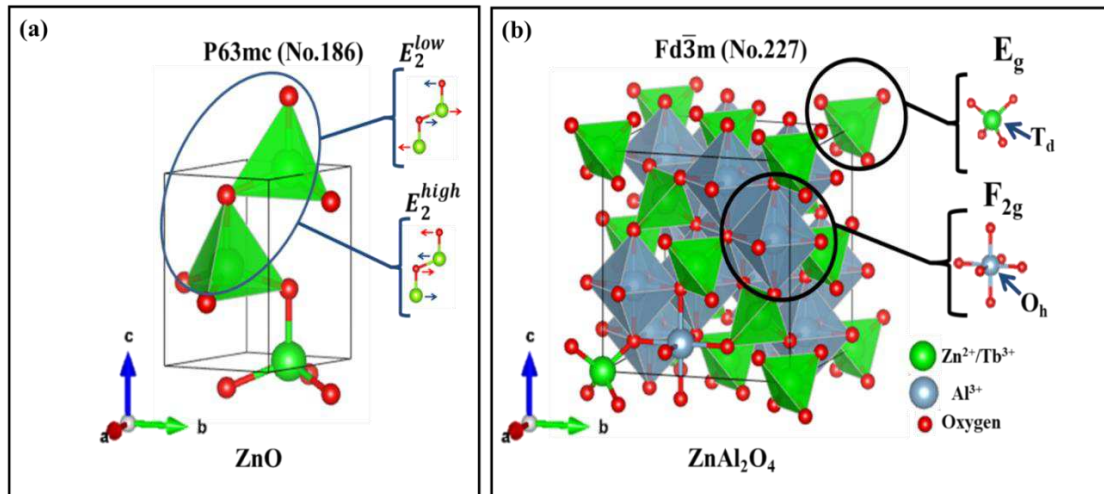


Fig. 2 Unit cell of the (a) ZnO and (b) ZnAl_2O_4 with atom vibrational schematic

Analysis of the most intense diffraction peaks (101) and (311) from the ZnO and ZnAl_2O_4 phases are shown in Fig. 3. Fig. 3 (a) shows the decrease of the ZnO (101) diffraction peak intensity with an increase of Al_x moles and completely disappears at $x = 1.5$, and this signifies the extermination of the ZnO phase. The increase of the ZnAl_2O_4 (311) diffraction peak intensity for $x < 1.5$ suggest an increase in the crystallinity (or formation) of the ZnAl_2O_4 phase as Al_x moles increases up to $x = 1.5$. This is due

to the availability of enough Al atoms to form ZnAl₂O₄ single phase. As x increases beyond 1.5 the ZnAl₂O₄ phase diffraction intensity seems to be decreasing since the excess Al might possibly be incorporated within the ZnAl₂O₄ matrix, which leads to the absence of alumina (Al₂O₃) related diffraction patterns. The excess Al within ZnAl₂O₄ influenced the diffraction angle (see Fig. 3 (b)), which subsequently affect the lattice constant.

The stacked zoomed analysis of the ZnO (101) and ZnAl₂O₄ (311) displayed in Fig. 3 (b) shows that both peaks are shifting towards a lower diffraction angle as x increases up to 1.5 resulting in the expansion of the lattice constant [9,15]. On the ZnAl₂O₄ phase, this can be caused by the excess Zn²⁺ into ZnAl₂O₄ crystal lattice, as for the ZnO phase, the lattice constant increases due to multiple incorporation of Al³⁺ ion and/or Zn intrastitial within the ZnO matrix which intend pave the formation of single phase ZnAl₂O₄. When x ≥ 1.5, the (311) diffraction peak shifts towards higher diffraction angle signifying a decrease in lattice constant. Meaning that some of the Al³⁺ (ionic radius = 0.53 Å [7,34]) are occupying the Zn²⁺ (ionic radius = 0.74 Å [9,34]) site. This behaviour can be explained using the Vegard's law [35,36] which suggests that the substitution or replacement of a certain ion with the smaller or bigger ionic radius is expected to shrink or expand the lattice constant, respectively. The lattice constant of the ZnAl₂O₄ and ZnO were respectively estimated using the equation (1) [9,12] and (2) [9,37]

$$\frac{1}{d_{hkl}^2} = \frac{h^2+k^2+l^2}{a^2} \quad \dots (1)$$

$$\frac{1}{d_{hkl}^2} = \frac{4}{3} \left(\frac{h^2+hk+k^2}{a^2} + \frac{l^2}{c^2} \right) \quad \dots (2)$$

where *a* and *c* are the lattice constant, *d* is the interplanar distance and *hkl* are the miller indices. The lattice constant (*a*) for ZnAl₂O₄ were calculated from the (311) diffraction peaks. The lattice constant (*a*) and (*c*) for ZnO were calculated from the (002) and (101) diffraction peaks, respectively. The estimated lattice constant for both the ZnO and ZnAl₂O₄ are presented in Table 1 and they are in agreement with those previously reported values in literature by the Refs [25,37–39]. The average lattice constants *a* = *b* and *c* for ZnO are 2.836 and 5.158 Å, respectively, and ZnAl₂O₄ average lattice

constants is $a = b = c = 8.011 \text{ \AA}$. The lattice constant as a function of Al_x moles is depicted in Fig. 4 (a). The lattice constant increase from $x = 0.25$ to 1 due to the excess of Zn atoms compared to Al atoms, the dramatic decrease to $x = 1.5$ is due to the completely removal of ZnO phase due to reasonable Zn:Al ratio to start forming ZnAl_2O_4 single phase. An increase in lattice parameters from $x = 1.5$ to 2.5 might be attributed to the full formation of stable ZnAl_2O_4 single phase. The observed decrease in lattice parameter at $x > 2.5$ might be due to Al^{3+} replacing the Zn^{2+} ions in ZnAl_2O_4 crystal lattice.

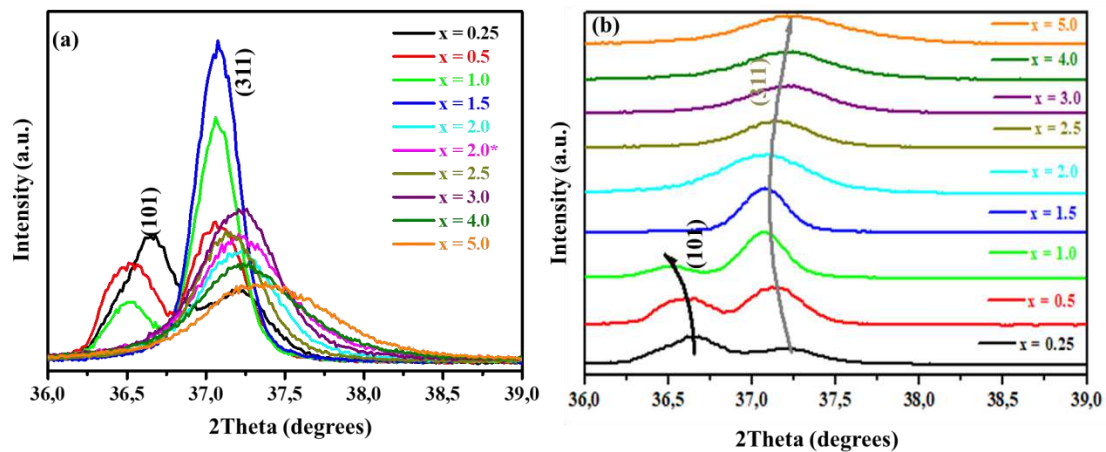


Fig. 3 Zoomed analysis of diffraction peak (a) intensity and (b) shift of the (101) ZnO and (311) ZnAl_2O_4 phase of $\text{ZnAl}_x\text{O}_{1.5x+1} : 0.1\% \text{ Tb}^{3+}$ ($0.25 \leq x \leq 5.0$)

The crystallite size for the ZnO and ZnAl_2O_4 were estimated from the dominant diffraction peaks ZnO (101) and ZnAl_2O_4 (311) using Scherrer's formula [40]. The estimated values are presented in Table 1. The crystallite size of the ZnAl_2O_4 as a function of Al_x mole is presented on Fig. 4 (a). The graph of crystallite resembles a similar behaviour as that of the lattice constant. The strain on the ZnAl_2O_4 and ZnO phases was calculated from Williams and Hall method [41], and the values are presented in Table 1. Strain as a function of the Al_x is shown in Fig. 4 (b). When $0.25 \geq x > 1.0$ the strain decreases due to multiple phases present in the ZAOT system and that it is easy to form both the ZnO and ZnAl_2O_4 . At $x = 1.5$, the strain increases due to the formation of ZnAl_2O_4 single phase. At the decrease in strain above $x > 1.5$ is probably due to easy formation of ZnAl_2O_4 at

these Al_x moles. Above $x \geq 2.5$, the strain increases linearly as more Al ions are being incorporated into the $ZnAl_2O_4$ matrix.

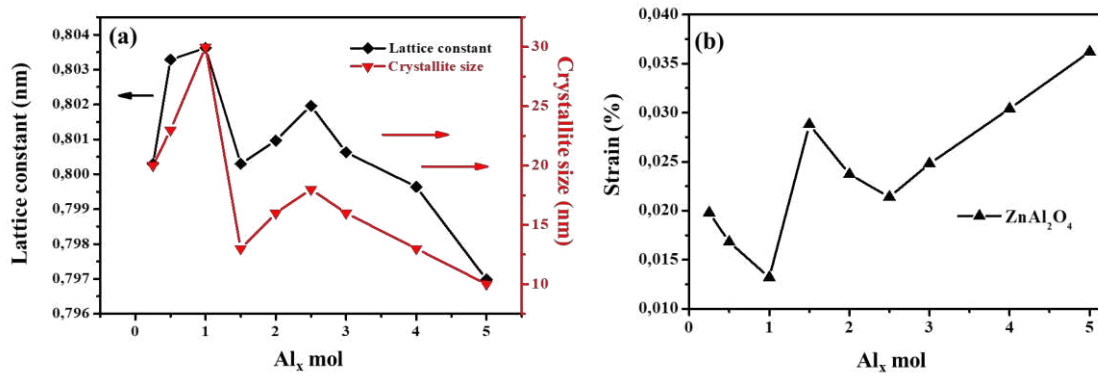


Fig. 4 The (a) lattice constant and crystallite size (nm); and (b) strain of $ZnAl_2O_4$ phase as a function of Al_x mol

Table 1. Sample identification, strain, lattice constant and crystallites size of ZnO and $ZnAl_2O_4$.

Sample ID	Quantification (%)		Lattice parameter (Å)			Crystallite Size (nm)		Strain (%)	
	ZnO	$ZnAl_2O_4$	ZnO	$ZnAl_2O_4$	$ZnAl_2O_4$	ZnO	$ZnAl_2O_4$	ZnO	$ZnAl_2O_4$
x			$a(\text{Å})$	$c(\text{Å})$	$a(\text{Å})$				
0.25	47.6	52.4	2.830	5.147	8.003	22	20	0.0182	0.0223
0.5	30.8	69.2	2.839	5.163	8.033	25	23	0.0156	0.0189
1.0	13.7	86.3	2.839	5.164	8.036	24	30	0.0166	0.0148
1.5	-	100	-	-	8.003	-	13	-	0.0323
2.0	-	100	-	-	8.010	-	16	-	0.0267
2.0*	-	100	-	-	8.033	-	30	-	0.0144
2.5	-	100	-	-	8.020	-	18	-	0.0240
3.0	-	100	-	-	8.006	-	16	-	0.0279
4.0	-	100	-	-	7.996	-	13	-	0.0342
5.0	-	100	-	-	7.970	-	10	-	0.0407

(* denotes un-doped sample, y is the estimated oxygen mole moles)

3.2. Raman Spectroscopy

Raman spectroscopy was employed to identify the molecular structure of the prepared samples and the obtained spectra are shown in Fig. 5. The results show that there are five Raman peaks located at 62, 101, 420, 440 and 660 cm^{-1} . The peaks at 101 and 440 cm^{-1} are attributed to the ZnO phase specifically from the E_2^{low} and E_2^{high} resulting from the Zn and O atomic oscillations (see Fig. 2 (a)) [42,43]. These peaks disappear at $x > 1.5$, which is a clear confirmation that they are indeed from ZnO phase as it was suggested by the XRD results in Fig. 1. The Raman peaks at 420 and 660 cm^{-1} are due to ZnAl_2O_4 . It is generally accepted that Raman modes within the medium frequency range (300-600 cm^{-1}) modes are due to the MO_6 octahedral while the high range frequency ($> 600 \text{ cm}^{-1}$) modes are due to the MO_4 tetrahedral. Thus, the 420 and 660 cm^{-1} bands can be attributed to the E_g and F_{2g} mode ascribed to the O_h and T_d site [20,21], respectively. These observed two peaks from ZnAl_2O_4 is in good agreement with the previous reports [16,17,20,21]. Previous studies [16,44] have shown that E_g and F_{2g} modes of Raman spectrum of the inverse spinel occurred in the 350 - 400 and 490 - 640 cm^{-1} region. $\text{Zn}_{0.9}\text{Cu}_{0.1}\text{Al}_2\text{O}_4$ and $\text{Zn}_{0.9}\text{Ni}_{0.1}\text{Al}_2\text{O}_4$ have also shown a lower frequency Raman shift located in the 395-410 and 630-650 cm^{-1} which was attributed to appearance of minor inverse spinel [16,20]. Therefore, these results suggest that the prepared ZnAl_2O_4 spinel has crystallised in the normal configuration. The Raman peak located at 62 cm^{-1} can be attributed to the Zn interstitial [43] and/or the presents of Tb^{3+} within the ZnO or ZnAl_2O_4 hosts matrix. The Raman confirms or revealed the structural transition from multiphase ZnO/ ZnAl_2O_4 to ZnAl_2O_4 single phase. Note that the intensity of the Raman peak at 62 cm^{-1} for the $x = 2.0$ (un-doped) sample is lower than the doped sample, which suggest that the Zn interstitial sites are more pronounced for the doped compared to the undoped sample [43]. Generally, the Raman and XRD result supports each other.

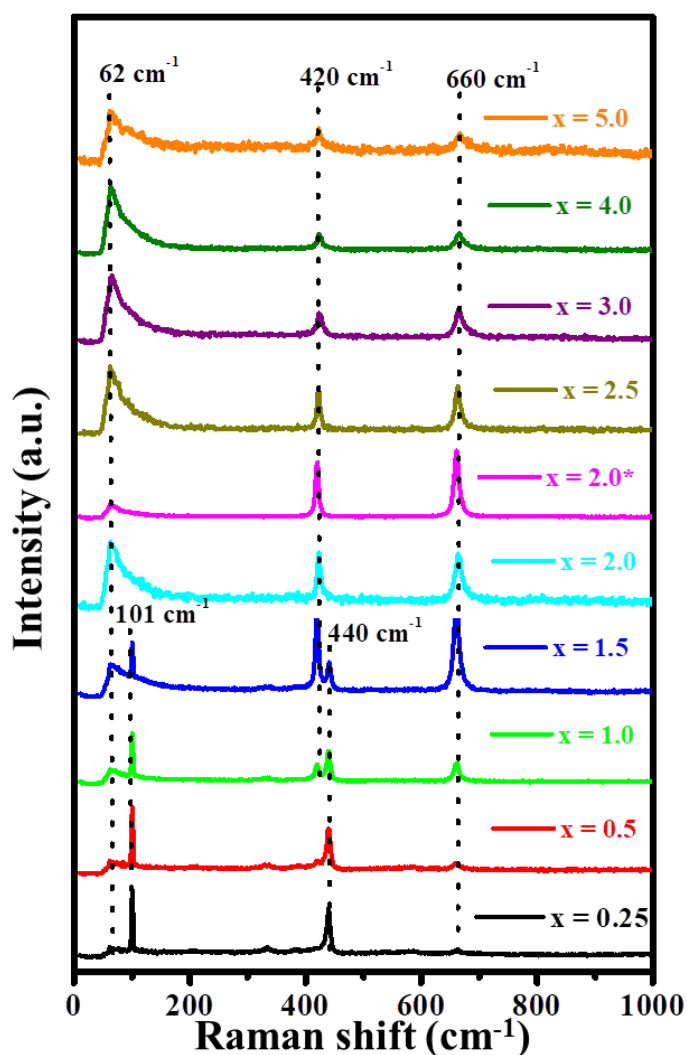


Fig. 5 The Spectra for the $x = 2.0^*$ (undoped) and $\text{ZnAl}_x\text{O}_{1.5x+1}:0.1\% \text{Tb}^{3+}$ ($0.25 \leq x \leq 5.0$)

3.3. Fourier-transform infrared spectroscopy

The FTIR spectra of the sample are depicted in Fig. 6. It is well known that infrared spectra of spinels are characterized by absorption band in the range between $400 - 700 \text{ cm}^{-1}$ [16,21]. The result shows that there are four bands at $479, 547, 656$ and 803 cm^{-1} . The three low occurring frequency bands are attributed to the vibration modes of normal ZnAl_2O_4 spinel. Several studies have attributed them to the following vibration modes: Al-O; asymmetric stretching, symmetric bending or symmetric stretching [45,46], respectively. Other studies have attributed them to Zn-O, Al-O and Zn-O-Al vibration [47–49]. These peaks are through-out the entire ZAOT samples because they all contain ZnAl_2O_4 phase as

observed on the XRD and Raman results. The additional absorption band at 803 cm^{-1} , which is clearly noticeable from $x \geq 3$ might be also from the ZnAl_2O_4 due to the Al-O bond arising from Al in the T_d site of ZnAl_2O_4 as suggest on the lattice constant and strain analysis.

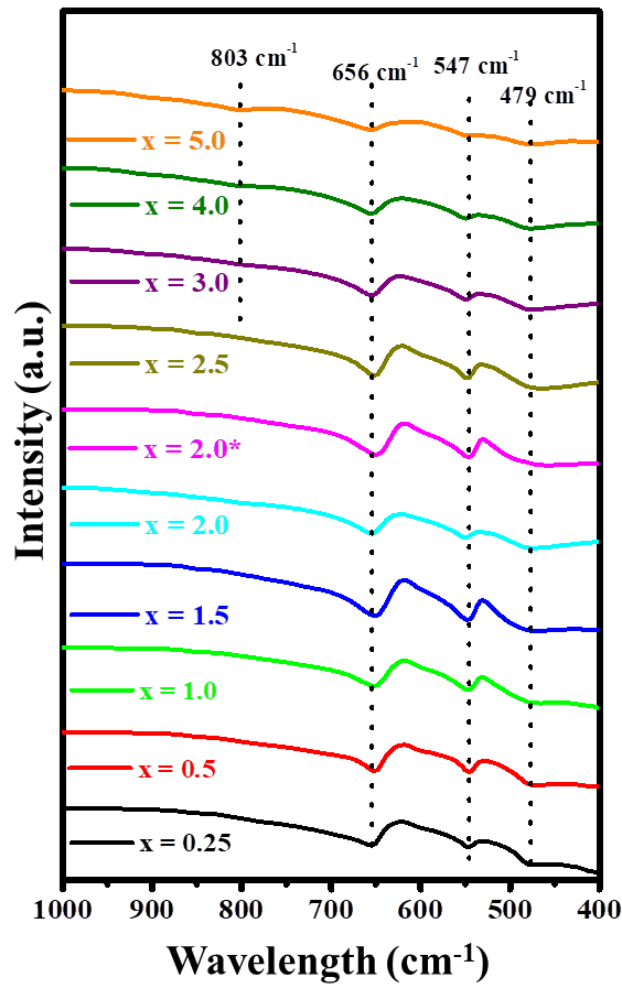


Fig. 6 The FTIR spectra for the $x = 2.0^*$ and $\text{ZnAl}_x\text{O}_{1.5x+1}:0.1\% \text{ Tb}^{3+}$ ($0.25 \leq x \leq 5.0$)

3.4. Energy-dispersive X-ray spectroscopy

The EDS technique was deployed to analyse the chemical composition of the un-doped and ZAOT nano-powders and the spectra for the selected is shown in Fig. 7. The expected elements namely Zn, Al, and O are observed in all spectra. Except for the element Tb, due to its low doping concentration. The additional peak of carbon (C) observed at the lower energy is due to the sample coating during the

sample preparation for the EDS analysis.

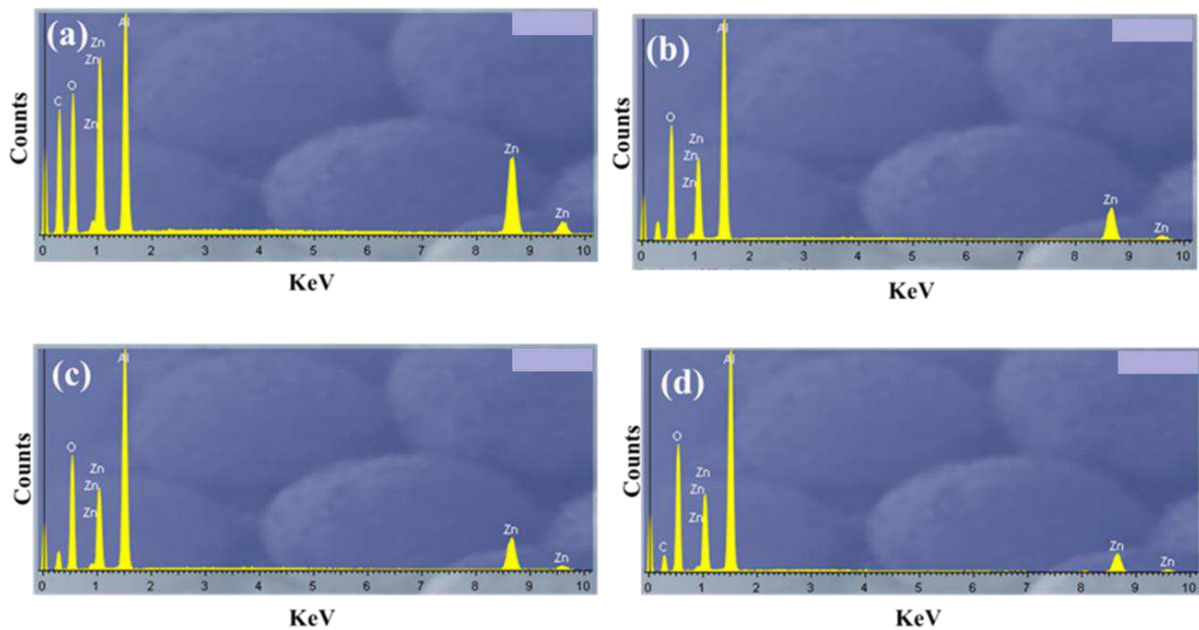


Fig. 7 The EDS spectrum of the $\text{ZnAl}_x\text{O}_{1.5x+1}:0.1\% \text{Tb}^{3+}$ where (a) $x = 0.25$, (b) 2.0* (un-doped), (c) 2.0, and (d) 4.0 nano-phosphors

3.5. Scanning Electron Microscopy

The SEM micrographs of the selected samples are shown in Fig. 8. The micrograph displayed on Fig. 8 (a) shows the $x = 0.25$, which is a dual morphology consisting of rods and randomly disturbed irregular crystallites. Arguing from the XRD and Raman results, the morphology of the spherical particles can be attributed to the ZnAl_2O_4 since it is observed in all sample as shown in Fig. 8 (a) – (d). Therefore, the rods structures are possibly due to the ZnO as they are only present at the lower Al_x . It is also clear that Tb^{3+} doping and varying the Al_x moles does not influence the crystallites agglomeration.

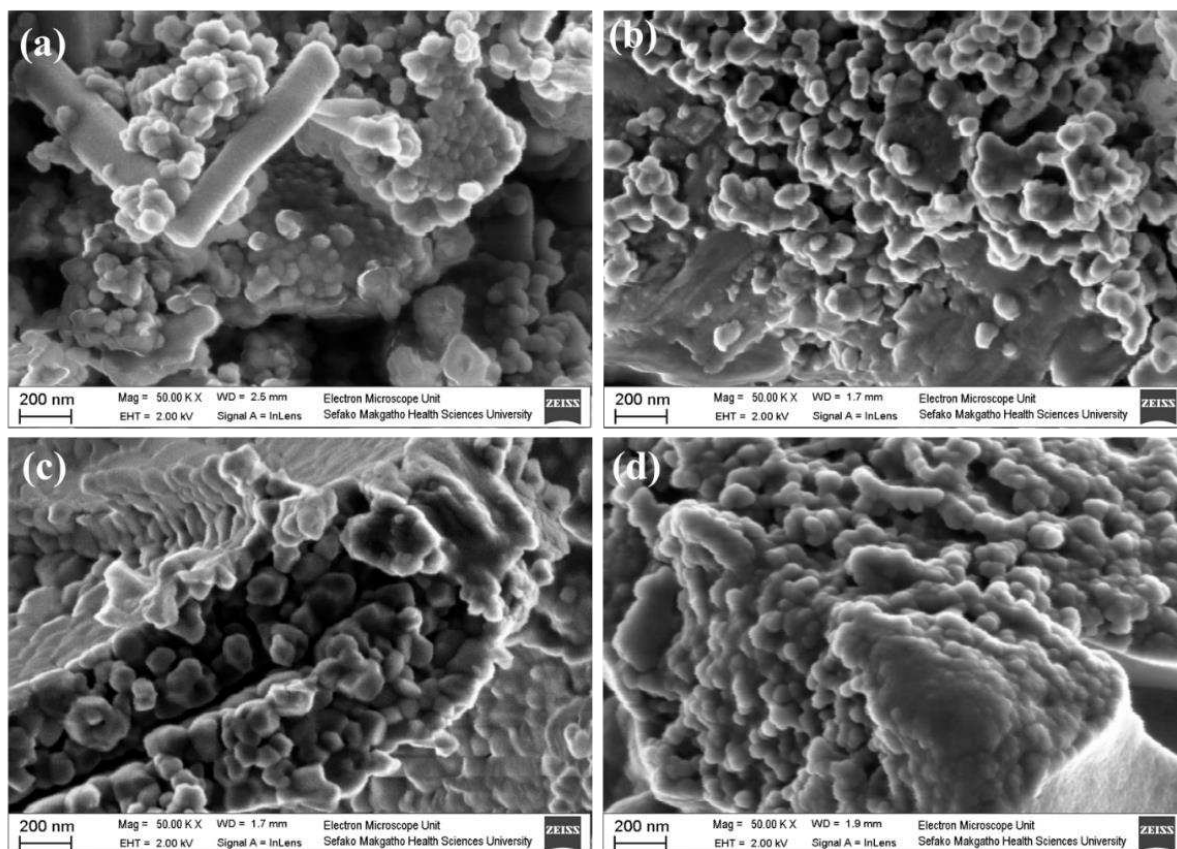


Fig. 8 The SEM micrographs of the (a) $x = 0.25$ (b) 2.0^* (un-doped) (c) 2.0 , and (d) 4.0 nano-phosphor

3.6. Transmission Electron Microscopy

The prepared samples were further analysed by the TEM to investigate the phase, crystal size and shapes. The TEM image of the selected samples is depicted in Fig. 9. In general, the TEM images confirm what has been observed in XRD, Raman and SEM in terms of the transition from dual morphology (or phase) to a single phase of ZnAl_2O_4 . The average particle size of the investigated nanopowders are in nanometric regime (i.e. below 30 nm), which agrees very well with the XRD results. In addition, the TEM images shows the presence of the hexagonal like-particles (indicated by the red arrows), which are certainly attributed to the ZnO. This results suggest that there might still be the presence of hexagonal ZnO phase at $x = 2.0$. However, the ZnO phase is totally vanished at higher Al_x moles (e.g. $x = 4.0$). Thus, TEM results also suggest the Al_x moles influenced the phase present on the prepared samples.

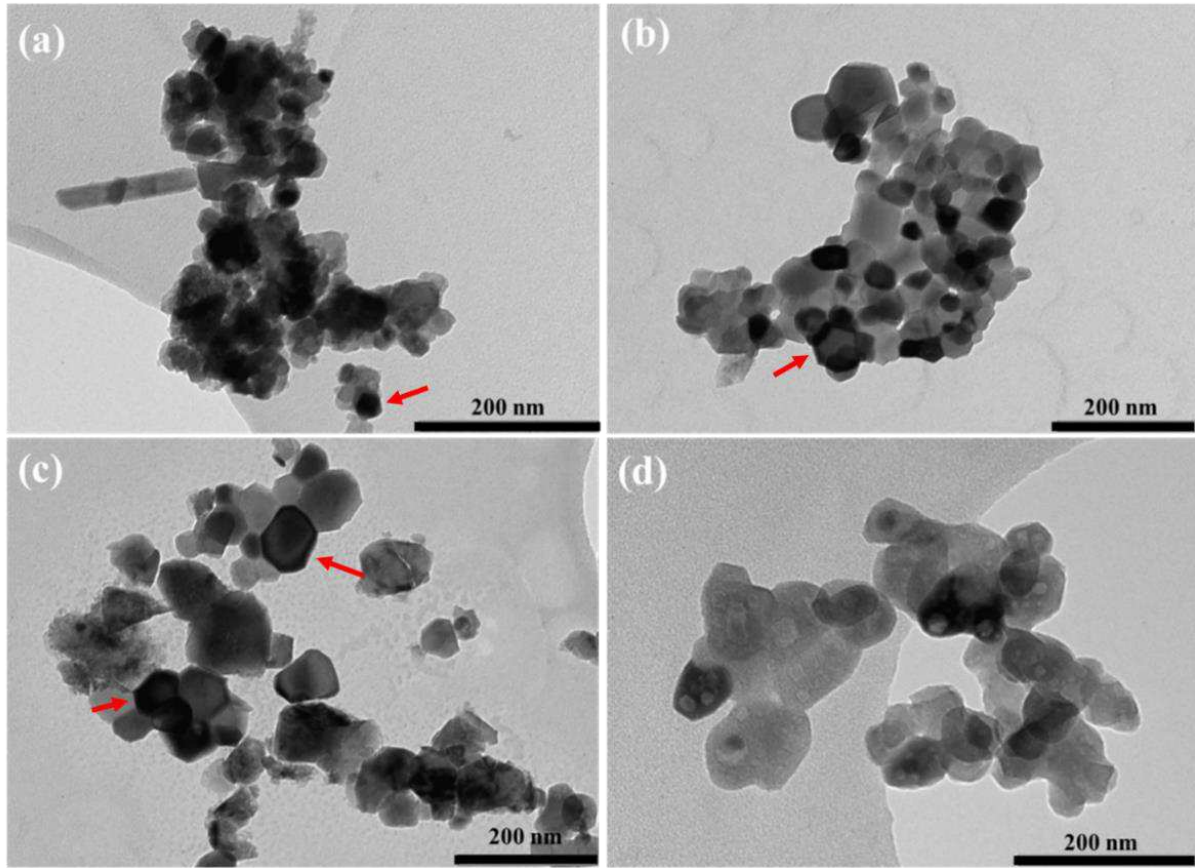


Fig. 9 The TEM micrographs of the (a) $x = 0.25$, (b) 2.0^* , (c) 2.0 , and (d) 4.0 nano-phosphor

3.7. Photoluminescence spectroscopy

The $\text{ZnAl}_x\text{O}_{1.5x+1}:0.1\% \text{Tb}^{3+}$ ($x = 2.0$) sample was excited at various excitation wavelength in a range of 200 – 280 nm and the obtained emission spectra is illustrated in Fig. 10 (a). The emission spectra show the presence of eight emission peaks located at 382, 414, 439, 458, 489, 545, 585 and 621 nm, which can be attributed to the $^5\text{D}_3 \rightarrow ^7\text{F}_6$, $^5\text{D}_3 \rightarrow ^7\text{F}_5$, $^5\text{D}_3 \rightarrow ^7\text{F}_4$, $^5\text{D}_3 \rightarrow ^7\text{F}_2$, $^5\text{D}_4 \rightarrow ^7\text{F}_6$, $^5\text{D}_4 \rightarrow ^7\text{F}_5$, $^5\text{D}_4 \rightarrow ^7\text{F}_4$ and $^5\text{D}_4 \rightarrow ^7\text{F}_3$ transitions of Tb^{3+} [23,27,41,50,51], respectively. The usual emissions at 398 nm from the ZnAl_2O_4 host was not detected and this might be due to the high annealing temperature used in this study which quenched the luminescence active traps within the ZnAl_2O_4 [19]. Singh et al. [19] results showed that the luminescence active defects within ZnAl_2O_4 decreases dramatically after the annealing temperature of 600 °C. The emission intensity of the most intense peak at 545 nm as a function of excitation wavelength is shown in Fig. 10 (b), which shows a Gaussian behaviour. The Gaussian fit

results shows that the optimum excitation wavelength is at 225 nm. This might probably serve as a good reason why a similar excitation wavelength of 228 nm was used to excite the $\text{ZnAl}_2\text{O}_4:4 \text{ mol. } \% \text{ Tb}^{3+}$ system [51].

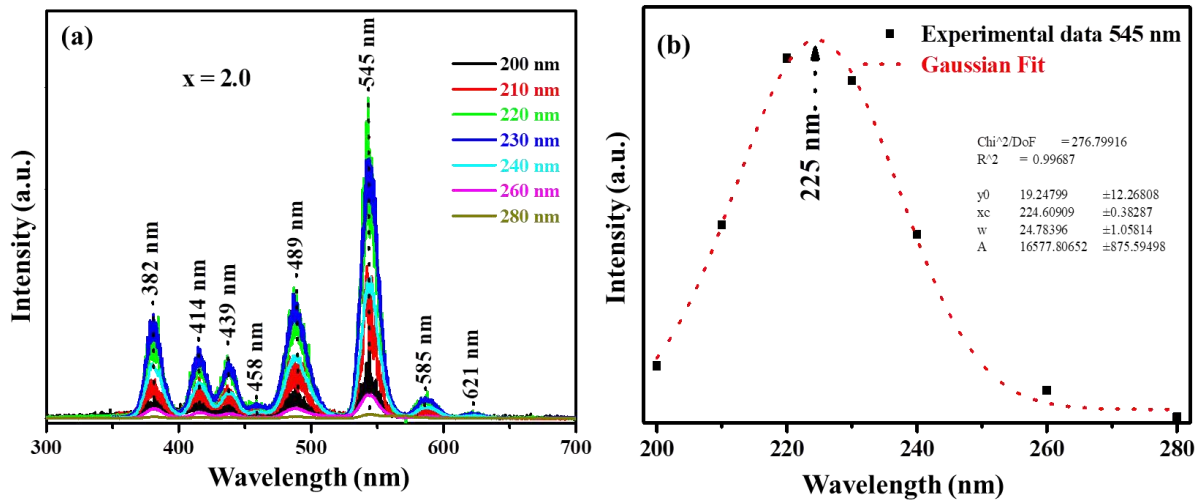


Fig. 10 (a) The emission spectra of the $x = 2.0$ sample excited at various excitation wavelength and (b) emission intensity as a function of excitation wavelength

The RT PL excitation and emission spectra of the $x = 2.0^*$ and ZAOT series are presented in Fig. 11. The excitation spectra of the un-doped ($x = 2.0^*$) and doped ($x = 2.0$) displayed on Fig. 11 (a) were measured when monitoring the 545 nm emission which shows the presences of a broad excitation band located at 225 nm. This excitation band at 225 nm can be attributed to the spin allowed transition ($\Delta S = 0$) from the $4F^8$ (ground state) $\rightarrow 4F^75d^1$ of the Tb^{3+} ions [27]. The emission spectra show the presences of eight peaks which were similar to those observed in Fig. 10 (a). To further investigate the emissions originating from the un-doped, the emission spectra of the doped $x = 2.0$ and un-doped $x = 2.0$ samples were normalized as shown in Fig. 11 (b). Fig. 11 (c) shows the deconvolution emission spectra of the un-doped ($x = 2.0^*$) sample. From Fig. 11 (b), the excitation band is most likely to be due to the band-to-band transition of AlO_6 anion grouping in ZnAl_2O_4 [52]. From Fig. 11 (c), the observed emission bands from the host at 407 nm can be ascribed to the intrinsic intraband gap defects, such as oxygen vacancies (Vo^*) [52]. The 458 nm peak can be ascribed to the second order of 225 nm excitation

wavelength. Based on the TEM results for the $x = 2.0$ and $x = 2.0^*$ (and all samples with ZnO phase), it is therefore reasonable to also attribute the 545 nm emission peak to the deep level defect emission within ZnO nanorods [53]. Since the ZnO might still be present although at the small proportions. The excitation and emission spectrums of the ZAOT series is shown in Fig. 11 (d). The results show that there were no new emission peaks which were observed except the ones discussed in Figs. 10 and 11 (a). It is important to emphasize that the 458 nm emission peak is attributed to both the contribution from Tb^{3+} ($^5D_3 \rightarrow ^7F_2$ transition) and second order emission. The most intense emission peak at 545 nm is attributed to a magnetic dipole transition which hardly varies in the presents of crystal field strength, while the 489 nm ascribed to the electrical dipole which is sensitive to the local environment and depends on the symmetry of the crystal field [27,54]. Fig. 11 (e) shows the emission intensity of the 545 nm emission peak as a function of Al_x moles. The result shows a dramatic increase in the emission intensity when $x > 1.5$, which can be attributed to the multiphase change to single phase on the prepared phosphors. Furthermore, the results imply that the presence of the ZnO at high quantities quenches the luminescence.

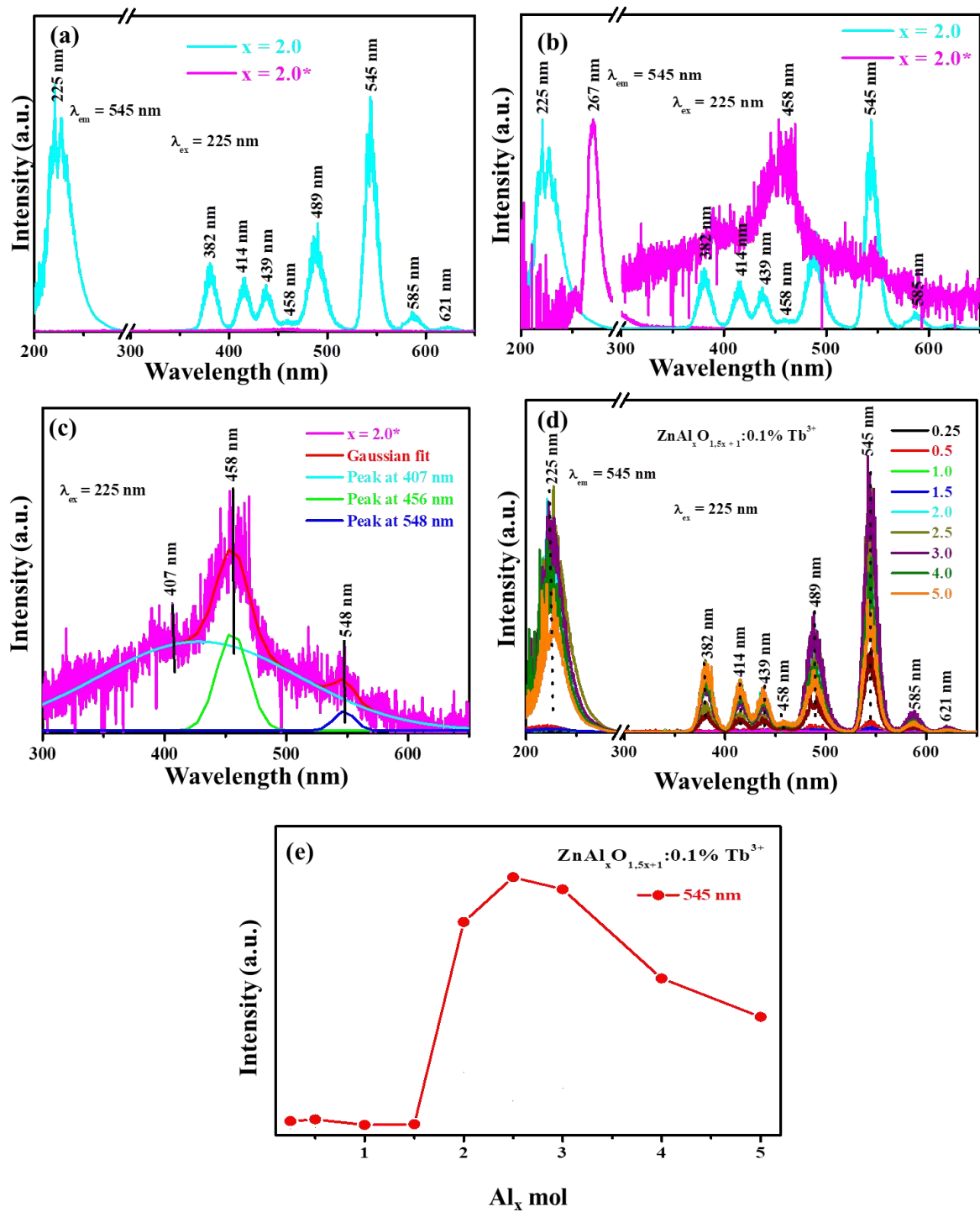


Fig. 11 Excitation and emission spectra of the (a) un-doped ($x = 2.0^*$) and doped ($x = 2.0$), (b) normalized of un-doped and doped, (c) deconvolution of the un-doped emission, (d) $\text{ZnAl}_x\text{O}_{1.5x+1}:0.1\% \text{Tb}^{3+}$ ($0.25 \leq x \leq 5.0$), and (e) emission intensity of the peak located at 545 nm as a function of Al_x moles.

In order to properly deduce the transitions within the band gap, the most intense sample $x = 2.5$ ($\text{ZnAl}_{2.5}\text{O}_{4.75}:0.1\% \text{Tb}^{3+}$) was further examined by monitoring excitation of each emission bands. Fig. 12 (a) shows the obtained excitation for each individual emission peak. Fig. 12 (b) shows an additional excitation band located at 308 nm when monitoring an emission peak at 621 nm (insert shows the zoomed version for the wavelength range of 365 – 650 nm. The new absorption peak might be from the transition of Tb^{3+} arising from the ground state to the $^5\text{D}_4$ level. All the observed emission peaks are similar to those discussed in Fig. 10 and 11. The proposed pathway channels for the excitations and emissions discussed in this paper are shown in Fig. 13. The energy level location of Tb^{3+} within ZnAl_2O_4 was predicted based on the Dorenbo's diagram [26,55]. Note that the deep level defect emission within ZnO at 545 nm [58] is not shown on the excitation and emission pathway mechanism because it is only present on the samples with ZnO phase.

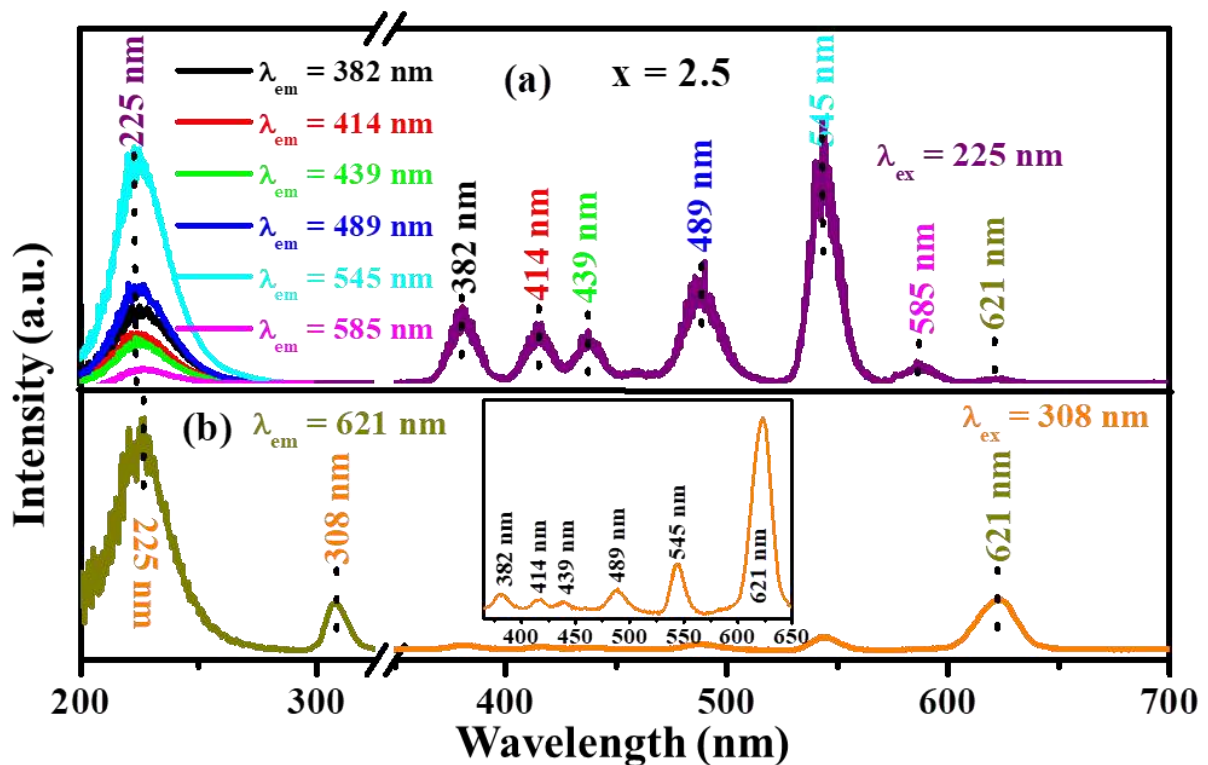


Fig. 12 Excitation and emission spectra of the $x = 2.5$ sample

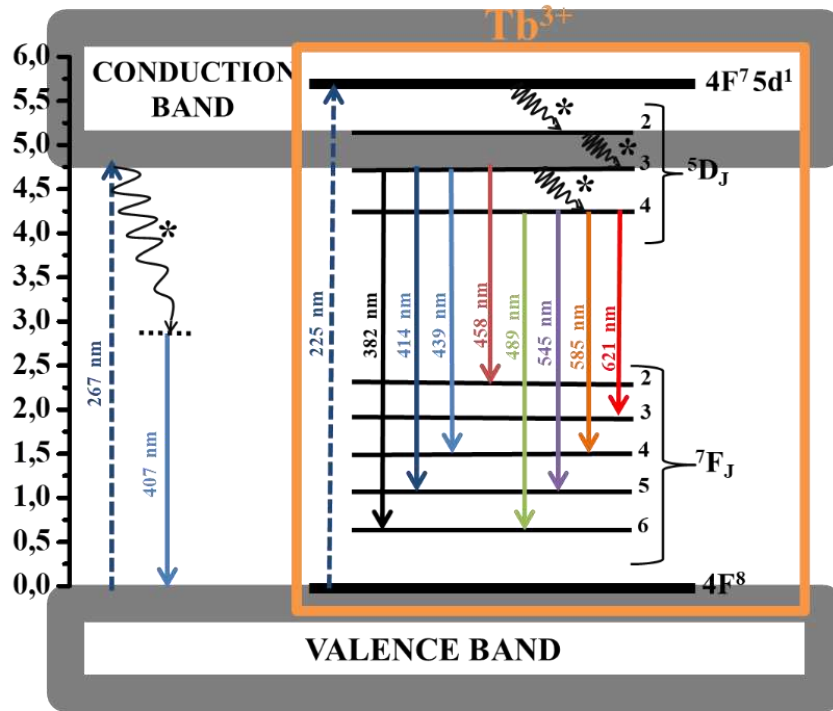


Fig. 13 The proposed excitation and emission pathways mechanism for ZnAl₂O₄:0.1%Tb³⁺ series

3.8. Lifetime

Fig. 14 shows the RT phosphorescence lifetime of the prepared ZAOT series. The lifetime was taken when monitoring the 545 nm emission wavelength and 225 nm excitation wavelengths. Fig. 14 (b) shows the natural logarithm of the lifetime intensity as a function of time. All the samples were fitted using the first order exponential decay presented on equation 3 [26,56].

$$I(t) = Ae^{(-t/\tau)} \quad \dots (3)$$

where I represents the phosphorescent intensity, A is the fitting parameters, t is the time of measurement and τ_1 time values. The fitting parameter and decay times are presented in Table 2.

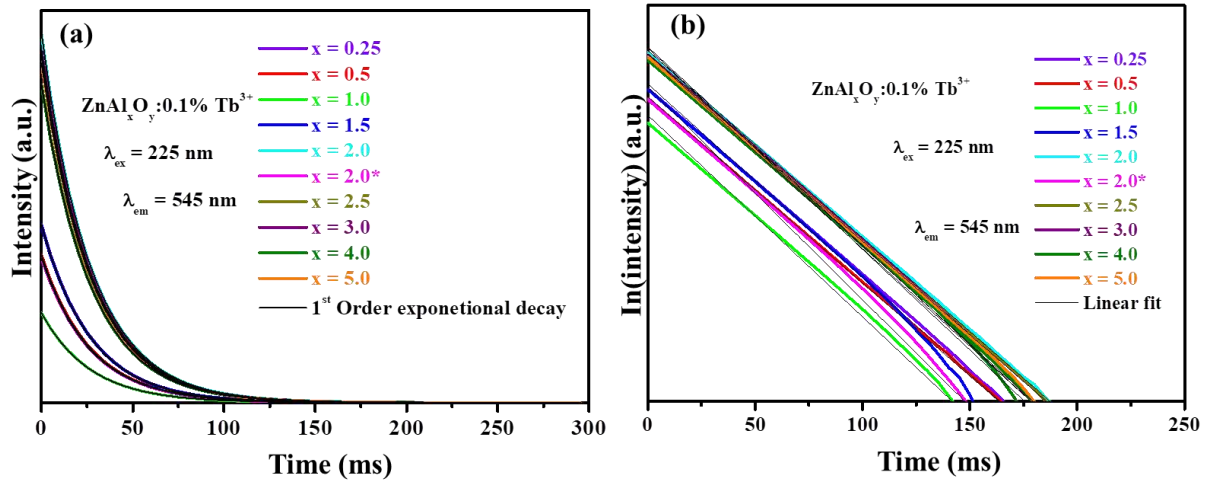


Fig. 14 (a) The decay curve and the (b) natural logarithm of the decay curve of host at $x = 2.0$ and $\text{ZnAl}_x\text{O}_y:0.1\%\text{Tb}^{3+}$ ($0.25 \leq x \leq 5.0$)

Table 2. Sample identification of fitting parameter, decay times and CIE colour coordinates.

Sample ID	fitting parameter	decay times (ms)	CIE
X	A_1	τ_1	(x;y)
0.25	4092.56 ± 0.92	26.82 ± 0.01	(0.143;0.378)
0.5	3385.24 ± 0.35	26.87 ± 0.00	(0.232;0.378)
1.0	2056.75 ± 1.79	26.74 ± 0.03	(0.231;0.308)
1.5	4067.85 ± 4.28	26.71 ± 0.04	(0.201;0.296)
2.0	8493.06 ± 2.00	26.94 ± 0.01	(0.232;0.455)
2.0*	3309.75 ± 3.45	26.63 ± 0.04	(0.153;0.147)
2.5	7974.16 ± 1.77	26.89 ± 0.01	(0.243;0.531)
3.0	8096.12 ± 2.59	26.87 ± 0.01	(0.238;0.502)

4.0	7310.85 ± 1.80	26.85 ± 0.01	(0.223;0.429)
5.0	7814.12 ± 1.73	26.84 ± 0.01	(0.219;0.397)

Asterisk (*) denotes the un-doped

3.9. Colour chromaticity

The International Commission on Illumination (CIE) chromaticity diagram with vertex region of different colour and the co-ordinates of the luminescent material are displayed in Fig. 15. The colour co-ordinates of the prepared sample were calculated using the CIE co-ordinate calculator software [59]. The colour co-ordinates for the $x = 2.0$ sample excited at different excitation wavelength is shown in Fig. 15 (a). The results show that the excitation wavelength influence the emission colour. Fig. 15 (b) compare the emission colour co-ordinates of the un-dope and Tb^{3+} dope for $x = 2.0$ sample. The un-doped sample shows a blue colour emission while the Tb^{3+} doped shows the green emission, which clearly shows that doping influences the emission of the host material. The colour co-ordinates for the ZAOT series is shown in Fig. 15 (c) and the (x;y) values are also presented in Table 2. The results clearly show that varying the Al_x moles influence the emission colour. The emission colour could be tuned from greenish to bluish. Fig. 15 (d) shows the CIE colour co-ordinates for the $x = 2.5$ sample when excited at 225 and 308 nm. The results show that the emission colour highly depends on the excitation wavelength.

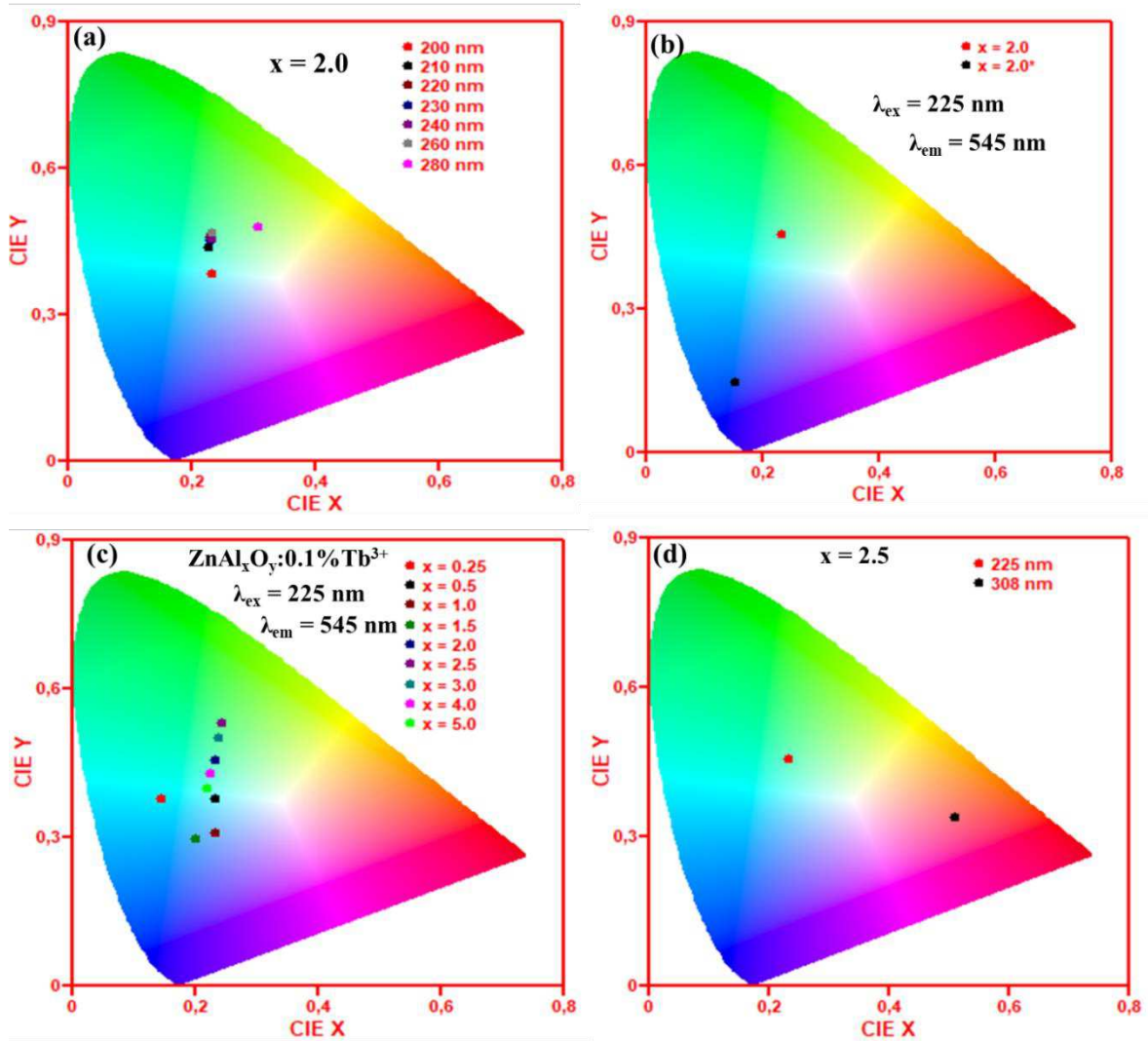


Fig. 15 CIE colour for the (a) $x = 2.0$ at various excitation wavelength, (b) Tb^{3+} doped and un-doped sample at $x = 2.0$, (c) ZAOT series, and (d) $x = 2.5$ at the excitation wavelength of 225 and 308 nm

4. Conclusion

ZAOT nano-powders were successfully synthesized via citrate sol-gel method. The XRD and Raman spectrum shows the presence of both the ZnO and $ZnAl_2O_4$ phases on the prepared materials, which highly depends on the Al_x moles. The crystallite sizes of the ZnO and $ZnAl_2O_4$ were found to be on the nanometric regime. The EDS confirmed the presence of Zn, Al, and O. The element Tb was not detected due to lower doping concentrations used in this study. The SEM showed that varying the Al_x moles

influence the morphology of the prepared nano-phosphor. The FTIR results show peaks related to normal ZnAl₂O₄ spinel. The PL analysis showed eight emission peaks which were attributed to the ⁵D_j (j = 3 and 4) → ⁷F_j (j = 3 - 6). The lifetime measurement showed that the prepared nano powders have similar decay mechanism. CIE colour chromaticity showed that varying Al_x moles and excitation wavelength significantly influence the emission colour.

Acknowledgements

This work is supported by the South African National Research Foundation (NRF) Thuthuka programme (fund number: UID 99266 and 113947) and NRF incentive funding for rated researchers (IPRR) (Grant No: 114924). The author would also like to acknowledge Miss. N. Thabane for assisting in sample synthesis. Dr James Wesley-Smith at Electron Microscopy Unit at Sefako Makgatho Health Science University is acknowledged for the SEM and TEM imaging.

References

- [1] M.A. Lahmer, The effect of Fe-doping on the electronic, optical and magnetic properties of ZnAl₂O₄; a first-principles study, *Comput. Condens. Matter.* **20**, e00387 (2019). <https://doi.org/10.1016/j.cocom.2019.e00387>
- [2] C.W. Cady, G. Gardner, Z.O. Maron, M. Retuerto, Y.B. Go, S. Segan, M. Greenblatt, G.C. Dismukes, Tuning the electrocatalytic water oxidation properties of AB₂O₄ spinel nanocrystals: A (Li, Mg, Zn) and B (Mn, Co) site variants of LiMn₂O₄, *ACS Catal.* **5**, 3403–3410 (2015). <https://doi.org/10.1021/acscatal.5b00265>
- [3] G. Yan, G. Li, H. Tan, Y. Gu, Y. Li, Spinel-type ternary multimetal hybrid oxides with porous hierarchical structure grown on Ni foam as large-current-density water oxidation electrocatalyst, *J. Alloys Compd.* **838**, 155662 (2020). <https://doi.org/10.1016/j.jallcom.2020.155662>

- [4] N.A. Masmali, Z. Osman, A.K. Arof, Recent developments in zinc-based two-cation oxide spinels: From synthesis to applications, *Ceram. Int.* **47**, 2949–2962 (2020). <https://doi.org/10.1016/j.ceramint.2020.09.249>
- [5] P. Kulkarni, R.G. Balkrishna, D. Ghosh, R.S. Rawat, R. Medwal, B.V.R. Chowdari, Z. Karim, M. V. Reddy, Molten salt synthesis of CoFe_2O_4 and its energy storage properties, *Mater. Chem. Phys.* **257**, 123747 (2021). <https://doi.org/10.1016/j.matchemphys.2020.123747>
- [6] K. Song, X. Chen, R. Yang, B. Zhang, X. Wang, P. Liu, J. Wang, Novel hierarchical $\text{CoFe}_2\text{Se}_4@ \text{CoFe}_2\text{O}_4$ and $\text{CoFe}_2\text{S}_4@ \text{CoFe}_2\text{O}_4$ core-shell nanoboxes electrode for high-performance electrochemical energy storage, *Chem. Eng. J.* **390**, 124175 (2020). <https://doi.org/10.1016/j.cej.2020.124175>
- [7] L.T. Melato, O.M. Ntwaeaborwa, R.E. Kroon, T.E. Motaung, S. V. Motloun, Effect of Ho^{3+} concentration on the structure, morphology and optical properties of $\text{Ba}_{0.5}\text{Mg}_{0.5}\text{Al}_2\text{O}_4$ nanophosphor, *J. Mol. Struct.* **1176**, 217–225 (2019). <https://doi.org/10.1016/j.molstruc.2018.08.093>
- [8] M.A. Malimabe, S. V. Motloun, T.E. Motaung, L.F. Koao, Effects of Eu^{3+} co-doping on the structural and optical properties of Ce^{3+} doped ZnO powder synthesized by chemical bath deposition method, *Phys. B Condens. Matter.* **579**, 411890 (2020). <https://doi.org/10.1016/j.physb.2019.411890>
- [9] V.M. Maphiri, J. Wesley-Smith, S. V. Motloun, Phase transition and optical properties of $\text{Ba}_{1-x}\text{Zn}_x\text{Al}_2\text{O}_4:0.1\% \text{Eu}^{3+}$ prepared via citrate sol-gel method, *J. Lumin.* **215**, 116710 (2019). <https://doi.org/10.1016/j.jlumin.2019.116710>
- [10] F.X. Jiang, R.X. Tong, Z. Yan, L.F. Ji, X.H. Xu, d-electron-dependent transparent conducting oxide of V-doped ZnO thin films, *J. Alloys Compd.* **822**, 153706 (2020). <https://doi.org/10.1016/j.jallcom.2020.153706>
- [11] B.K. Sarma, P. Rajkumar, Al-doped ZnO transparent conducting oxide with appealing electro-

- optical properties – Realization of indium free transparent conductors from sputtering targets with varying dopant concentrations, *Mater. Today Commun.* **23**, 1000870 (2020).
<https://doi.org/10.1016/j.mtcomm.2019.100870>
- [12] I. Miron, C. Enache, M. Vasile, I. Grozescu, Optical properties of ZnAl₂O₄ nanomaterials obtained by the hydrothermal method, *Phys. Scr.* **2012**, 014064 (2012).
<https://doi.org/10.1088/0031-8949/2012/T149/014064>
- [13] S. Atiq, M.T. Ansar, A. Hassan, S.K. Abbas, T. Iqbal, M. Aslam, M.J. Iqbal, A. Mahmood, Interlayer effect on photoluminescence enhancement and band gap modulation in Ga-doped ZnO thin films, *Superlattices Microstruct.* **144**, 106576 (2020).
<https://doi.org/10.1016/j.spmi.2020.106576>
- [14] T. Hussain, M. Junaid, S. Atiq, S.K. Abbas, S.M. Ramay, B.F. Alrayes, S. Naseem, Tunable dielectric behaviour and energy band gap range of ZnAl₂O₄ ceramics mediated by Mg substitution, *J. Alloys Compd.* **724**, 940–950 (2017).
<https://doi.org/10.1016/j.jallcom.2017.07.104>
- [15] V.M. Maphiri, F.B. Dejene, S. V. Motloug, Effects of Mg²⁺ concentration on the structure and optical properties of Mg_xAl₂O_{3+x}:0.88% Cd²⁺ (0.25 ≤ x ≤ 4.5) nano-powders synthesized via citrate sol-gel, *Results Phys.* **7**, 3510–3521 (2017). <https://doi.org/10.1016/j.rinp.2017.09.019>
- [16] V. D'Ippolito, G.B. Andreozzi, D. Bersani, P.P. Lottici, Raman fingerprint of chromate, aluminate and ferrite spinels, *J. Raman Spectrosc.* **46**, 1255–1264 (2015).
<https://doi.org/10.1002/jrs.4764>
- [17] M. Nasr, R. Viter, C. Eid, F. Warmont, R. Habchi, P. Miele, M. Bechelany, V. D'Ippolito, G.B. Andreozzi, D. Bersani, P.P. Lottici, Synthesis of novel ZnO/ZnAl₂O₄ multi co-centric nanotubes and their long-term stability in photocatalytic application, *RSC Adv.* **6**, 103692–103699 (2016).
<https://doi.org/10.1039/c6ra22623j>
- [18] S. V. Motloug, M. Tsega, F.B. Dejene, H.C. Swart, O.M. Ntwaeaborwa, L.F. Koao, T.E.

- Motaung, M.J. Hato, Effect of annealing temperature on structural and optical properties of $\text{ZnAl}_2\text{O}_4:1.5\% \text{Pb}^{2+}$ nanocrystals synthesized via sol-gel reaction, *J. Alloys Compd.* **677**, 72–79 (2016). <https://doi.org/10.1016/j.jallcom.2016.03.170>
- [19] V. Singh, N. Singh, M.S. Pathak, V. Dubey, P.K. Singh, Annealing effects on the luminescence properties of Ce doped ZnAl_2O_4 produced by combustion synthesis, *Optik* **155**, 285–291 (2018). <https://doi.org/10.1016/j.ijleo.2017.10.167>
- [20] J. Wang, A. Wang, D. Hu, X. Wu, Y. Liu, T. Chen, Synthesis, characterization and properties of Ni^{2+} -doped ZnAl_2O_4 -based spinel-type solid acid catalysts: $\text{SO}_4^{2-}/\text{Zn}_{1-x}\text{Ni}_x\text{Al}_2\text{O}_4$, *Mater. Chem. Phys.* **239**, 122319 (2020). <https://doi.org/10.1016/j.matchemphys.2019.122319>
- [21] V. Mohaček-Grošev, M. Vrankić, A. Maksimović, V. Mandić, Influence of titanium doping on the Raman spectra of nanocrystalline ZnAl_2O_4 , *J. Alloys Compd.* **697**, 90–95 (2017). <https://doi.org/10.1016/j.jallcom.2016.12.116>
- [22] C. Peng, G. Li, D. Geng, M. Shang, Z. Hou, J. Lin, Fabrication and luminescence properties of one-dimensional ZnAl_2O_4 and $\text{ZnAl}_2\text{O}_4: \text{A}^{3+}$ (A = Cr, Eu, Tb) microfibers by electrospinning method, *Mater. Res. Bull.* **47**, 3592–3599 (2012). <https://doi.org/10.1016/j.materresbull.2012.06.056>
- [23] G. Lakshminarayana, L. Wondraczek, Photoluminescence and energy transfer in $\text{Tb}^{3+}/\text{Mn}^{2+}$ co-doped ZnAl_2O_4 glass ceramics, *J. Solid State Chem.* **184**, 1931–1938 (2011). <https://doi.org/10.1016/j.jssc.2011.05.059>
- [24] E. Rusu, V. Ursaki, G. Novitschi, M. Vasile, P. Petrenco, L. Kulyuk, Luminescence properties of ZnGa_2O_4 and ZnAl_2O_4 spinels doped with Eu^{3+} and Tb^{3+} ions, *Phys. Status Solidi.* **6**, 1199–1202 (2009). <https://doi.org/10.1002/pssc.200881172>
- [25] S.V. Motloun, P. Kumari, L.F. Koao, T.E. Motaung, T.T. Hlatshwayo, M.J. Mochane, Effects of annealing time on the structure and optical properties of $\text{ZnAl}_2\text{O}_4/\text{ZnO}$ prepared via citrate sol-gel process, *Mater. Today Commun.* **14**, 294–301 (2018).

<https://doi.org/10.1016/j.mtcomm.2018.02.004>

- [26] S. V. Motloung, K.G. Tshabalala, R.E. Kroon, T.T. Hlatshwayo, M. Mlambo, S. Mpelane, Effect of Tb^{3+} concentration on the structure and optical properties of triply doped $ZnAl_2O_4:1\% Ce^{3+}, 1\% Eu^{3+}, x\% Tb^{3+}$ nano-phosphors synthesized via citrate sol-gel method, *J. Mol. Struct.* **1175**, 241–252 (2019). <https://doi.org/10.1016/j.molstruc.2018.08.002>
- [27] M. Kumar, S.K. Gupta, An insight into optical spectroscopy of intense green emitting $ZnAl_2O_4:Tb^{3+}$ nanoparticles: Photo, thermally stimulated luminescence and EPR study, *J. Lumin.* **168**, 151–157 (2015). <https://doi.org/10.1016/j.jlumin.2015.07.021>
- [28] M. Jain, Manju, A. Gundimeda, S. Kumar, G. Gupta, S.O. Won, K.H. Chae, A. Vij, A. Thakur, Defect induced broadband visible to near-infrared luminescence in $ZnAl_2O_4$ nanocrystals, *Appl. Surf. Sci.* **480**, 945–950 (2019). <https://doi.org/10.1016/j.apsusc.2019.02.198>
- [29] P. Kumari, Y. Dwivedi, Structural and photophysical investigations of bright yellow emitting $Dy: ZnAl_2O_4$ nanophosphor, *J. Lumin.* **178**, 407–413 (2016). <https://doi.org/10.1016/j.jlumin.2016.06.027>
- [30] J.C. Chen, C.T. Tang, Preparation and application of granular ZnO/Al_2O_3 catalyst for the removal of hazardous trichloroethylene, *J. Hazard. Mater.* **142**, 88–96 (2007). <https://doi.org/10.1016/j.jhazmat.2006.07.061>
- [31] T. Takemoto, D. He, Y. Teng, K. Tabata, E. Suzuki, E. Suzuki, Enhancement of methanol selectivity in the products of direct selective oxidation of methane in CH_4-O_2-NO with $Cu-ZnO/Al_2O_3$, *J. Catal.* **198**, 109–115 (2001). <https://doi.org/10.1006/jcat.2000.3119>
- [32] S. V. Motloung, F.B. Dejene, H.C. Swart, O.M. Ntwaeaborwa, Effects of Zn/citric acid mole fraction on the structure and luminescence properties of the un-doped and 1.5% Pb^{2+} doped $ZnAl_2O_4$ powders synthesized by citrate sol-gel method, *J. Lumin.* **163**, 8–16 (2015). <https://doi.org/10.1016/j.jlumin.2015.02.027>

- [33] K.Y. Chew, M.A. Bakar, N.H.H. Abu Bakar, Synthesis of Barium Nickel Titanium Oxide Stabilized by Citric Acid, *Model. Numer. Simul. Mater. Sci.* **03**, 23–27 (2013). <https://doi.org/10.4236/mnsms.2013.31b007>
- [34] V.M. Maphiri, Y. Dwivedi, L.F. Koao, R.E. Kroon, S. V. Motlounq, Analysis of varying Gd³⁺ concentrations on the structure and optical properties of ZnAl₂O₄:0.1% Eu³⁺; x% Gd³⁺ (0 ≤ x ≤ 1.2) synthesized via citrate sol–gel method, *Appl. Phys. A Mater. Sci. Process.* **126**, 73 (2020). <https://doi.org/10.1007/s00339-019-3260-y>
- [35] M.N. Magomedov, On the deviation from the Vegard’s law for the solid solutions, *Solid State Commun.* **322**, 114060 (2020). <https://doi.org/10.1016/j.ssc.2020.114060>
- [36] H.M. Foronda, B. Mazumder, E.C. Young, M.A. Laurent, Y. Li, S.P. DenBaars, J.S. Speck, Analysis of Vegard’s law for lattice matching In_xAl_{1-x}N to GaN by metalorganic chemical vapor deposition, *J. Cryst. Growth.* **475**, 127–135 (2017). <https://doi.org/10.1016/j.jcrysgro.2017.06.008>
- [37] M. Shahmirzaee, M. Shafiee Afarani, A.M. Arabi, A. Iran Nejjhad, In situ crystallization of ZnAl₂O₄/ZnO nanocomposite on alumina granule for photocatalytic purification of wastewater, *Res. Chem. Intermed.* **43**, 321–340 (2017). <https://doi.org/10.1007/s11164-016-2624-6>
- [38] G. Rani, Annealing effect on the structural, optical and thermoluminescent properties of ZnAl₂O₄:Cr³⁺, *Powder Technol.* **312**, 354–359 (2017). <https://doi.org/10.1016/j.powtec.2017.02.040>
- [39] W.M. Mulwa, B.F. Dejene, M.O. Onani, C.N.M. Ouma, Effect of Cu²⁺ doping on the structural, electronic and optical properties of ZnAl₂O₄: A combined experimental and DFT+U study, *J. Lumin.* **184**, 7–16 (2017). <https://doi.org/10.1016/j.jlumin.2016.12.008>
- [40] V.Y. Zenou, S. Bakardjieva, Microstructural analysis of undoped and moderately Sc-doped TiO₂ anatase nanoparticles using Scherrer equation and Debye function analysis, *Mater. Charact.* **144**, 287–296 (2018). <https://doi.org/10.1016/j.matchar.2018.07.022>

- [41] S. Som, S.K. Sharma, S.P. Lochab, Swift heavy ion induced structural and optical properties of $\text{Y}_2\text{O}_3:\text{Eu}^{3+}$ nanophosphor, *Mater. Res. Bull.* **48**, 844–851 (2013). <https://doi.org/10.1016/j.materresbull.2012.11.079>
- [42] Q.K. Doan, M.H. Nguyen, C.D. Sai, V.T. Pham, H.H. Mai, N.H. Pham, T.C. Bach, V.T. Nguyen, T.T. Nguyen, K.H. Ho, T.H. Tran, Enhanced optical properties of ZnO nanorods decorated with gold nanoparticles for self cleaning surface enhanced Raman applications, *Appl. Surf. Sci.* **505**, 144593 (2020). <https://doi.org/10.1016/j.apsusc.2019.144593>
- [43] Y. Song, S. Zhang, C. Zhang, Y. Yang, K. Lv, Raman Spectra and Microstructure of Zinc Oxide irradiated with Swift Heavy Ion, *Crystals* **9**, 395 (2019). <https://doi.org/10.3390/cryst9080395>
- [44] K.B. Modi, P.Y. Raval, S.J. Shah, C.R. Kathad, S. V. Dulera, M. V. Popat, K.B. Zankat, K.G. Saija, T.K. Pathak, N.H. Vasoya, V.K. Lakhani, U. Chandra, P.K. Jha, Raman and Mossbauer Spectroscopy and X-ray Diffractometry Studies on Quenched Copper–Ferri–Aluminates, *Inorg. Chem.* **54**, 1543–1555 (2015). <https://doi.org/10.1021/ic502497a>
- [45] S.F. Wang, G.Z. Sun, L.M. Fang, L. Lei, X. Xiang, X.T. Zu, A comparative study of ZnAl_2O_4 nanoparticles synthesized from different aluminum salts for use as fluorescence materials, *Sci. Rep.* **5**, 12849 (2015). <https://doi.org/10.1038/srep12849>
- [46] R. Peymanfar, F. Fazlalizadeh, Fabrication of expanded carbon microspheres/ ZnAl_2O_4 nanocomposite and investigation of its microwave, magnetic, and optical performance, *J. Alloys Compd.* **854**, 157273 (2021). <https://doi.org/10.1016/j.jallcom.2020.157273>
- [47] V.S. Kirankumar, S. Sumathi, Catalytic activity of bismuth doped zinc aluminate nanoparticles towards environmental remediation, *Mater. Res. Bull.* **93**, 74–82 (2017). <https://doi.org/10.1016/j.materresbull.2017.04.022>
- [48] Z. Zhu, X. Li, Q. Zhao, S. Liu, X. Hu, G. Chen, Facile solution synthesis and characterization of porous cubic-shaped superstructure of ZnAl_2O_4 , *Mater. Lett.* **65**, 194–197 (2011). <https://doi.org/10.1016/j.matlet.2010.09.085>

- [49] X. Li, Z. Zhu, Q. Zhao, L. Wang, Photocatalytic degradation of gaseous toluene over ZnAl_2O_4 prepared by different methods: A comparative study, *J. Hazard. Mater.* **186**, 2089–2096 (2011). <https://doi.org/10.1016/j.jhazmat.2010.12.111>
- [50] A.F.Y. Matsushita, A.A.C.C. Pais, A.J.M. Valente, Energy transfer and multicolour tunable emission of Eu,Tb(PSA)Phen composites, *Colloids Surfaces A Physicochem. Eng. Asp.* **569**, 93–101 (2019). <https://doi.org/10.1016/j.colsurfa.2019.02.049>
- [51] K.G. Tshabalala, I.M. Nagpure, H.C. Swart, O.M. Ntwaeaborwa, S.-H. Cho, J.-K. Park, Enhanced green emission from UV down-converting $\text{Ce}^{3+}\text{-Tb}^{3+}$ co-activated ZnAl_2O_4 phosphor, *J. Vac. Sci. Technol. B, Nanotechnol. Microelectron. Mater. Process. Meas. Phenom.* **30**, 031401 (2012). <https://doi.org/10.1116/1.3696720>
- [52] S. V. Motloung, F.B. Dejene, O.M. Ntwaeaborwa, H.C. Swart, Effects of catalyst/zinc mole fraction on $\text{ZnAl}_2\text{O}_4:0.01\% \text{Cr}^{3+}$ nanocrystals synthesized using sol-gel process, *Mater. Res. Express.* **1**, 045029 (2015). <https://doi.org/10.1088/2053-1591/1/4/045029>
- [53] J.C. Fan, S.L. Chang, Z. Xie, *ZnO-Based Light-Emitting Diodes*, Book chapter (2013). <https://doi.org/10.5772/51181>
- [54] S.K. Gupta, P.S. Ghosh, A. Arya, V. Natarajan, Origin of blue emission in ThO_2 nanorods: Exploring it as a host for photoluminescence of Eu^{3+} , Tb^{3+} and Dy^{3+} , *RSC Adv.* **4**, 51244–51255 (2014). <https://doi.org/10.1039/c4ra09681a>
- [55] P. Dorenbos, Electronic structure engineering of lanthanide activated materials, *J. Mater. Chem.* **22**, 22344–22349 (2012). <https://doi.org/10.1039/c2jm34252a>
- [56] J.I. Eldridge, Luminescence decay-based $\text{Y}_2\text{O}_3:\text{Er}$ phosphor thermometry: Temperature sensitivity governed by multiphonon emission with an effective phonon energy transition, *J. Lumin.* **214**, 116535 (2019). <https://doi.org/10.1016/j.jlumin.2019.116535>
- [59] <http://www.mathworks.com/matlabcentral/fileexchange/29620-cie-coordinate-calculator>

2012.

Figures

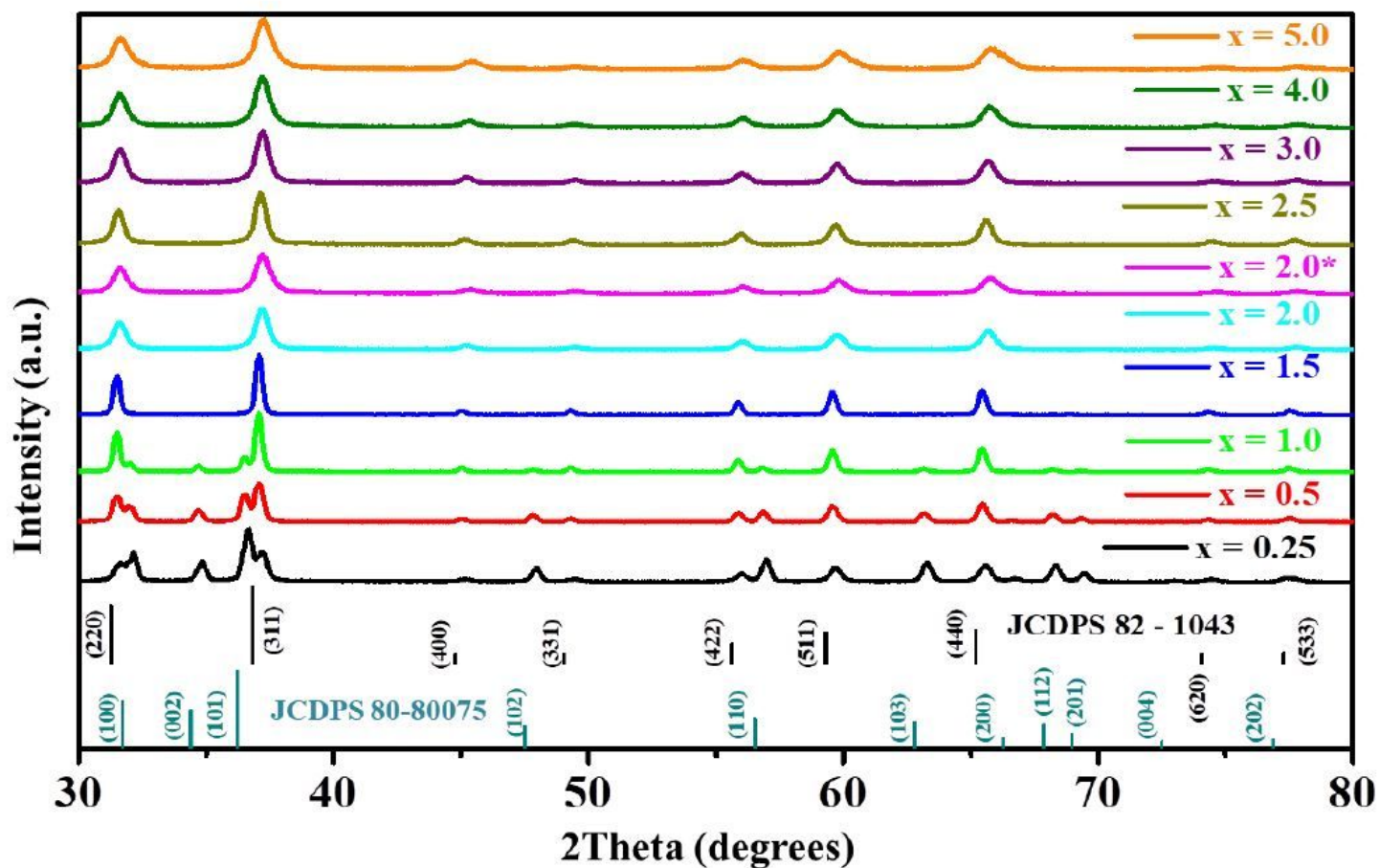


Figure 1

The XRD pattern for the $x = 2.0^*$ (un-doped) and ZnAl_xO_{1.5x} + 1:0.1% Tb³⁺ ($0.25 \leq x \leq 5.0$)

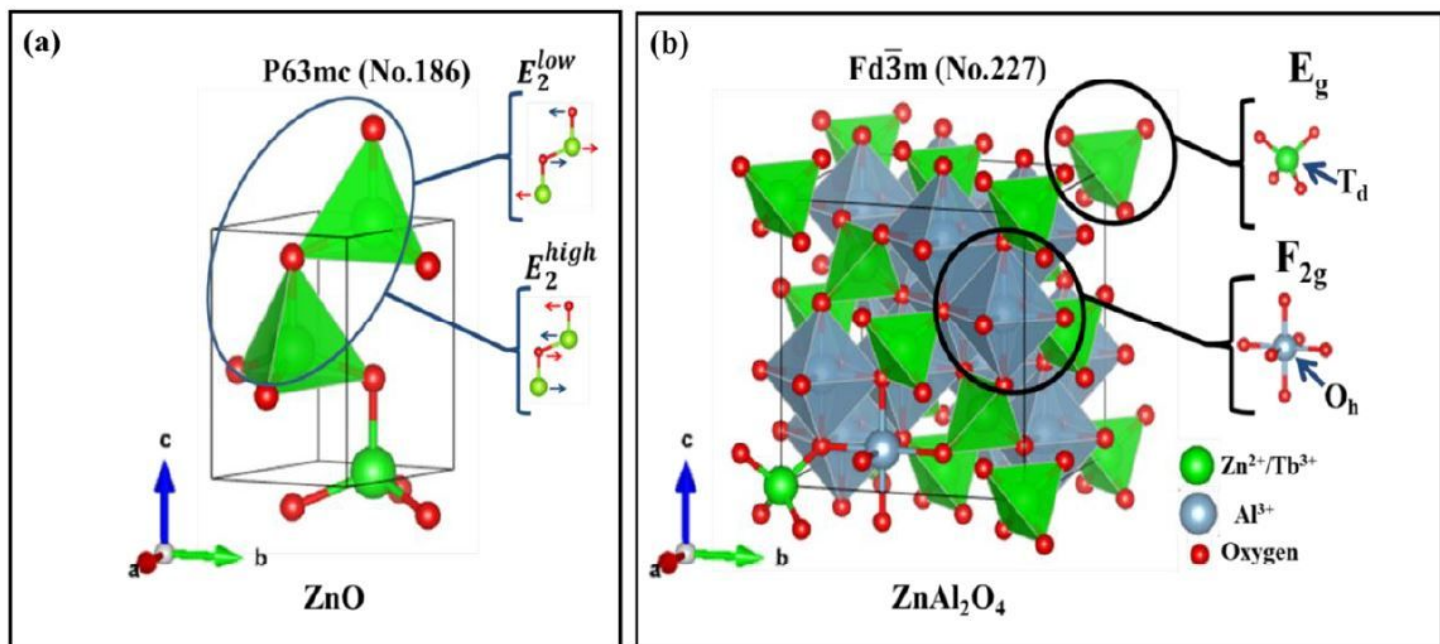


Figure 2

Unit cell of the (a) ZnO and (b) ZnAl₂O₄ with atom vibrational schematic

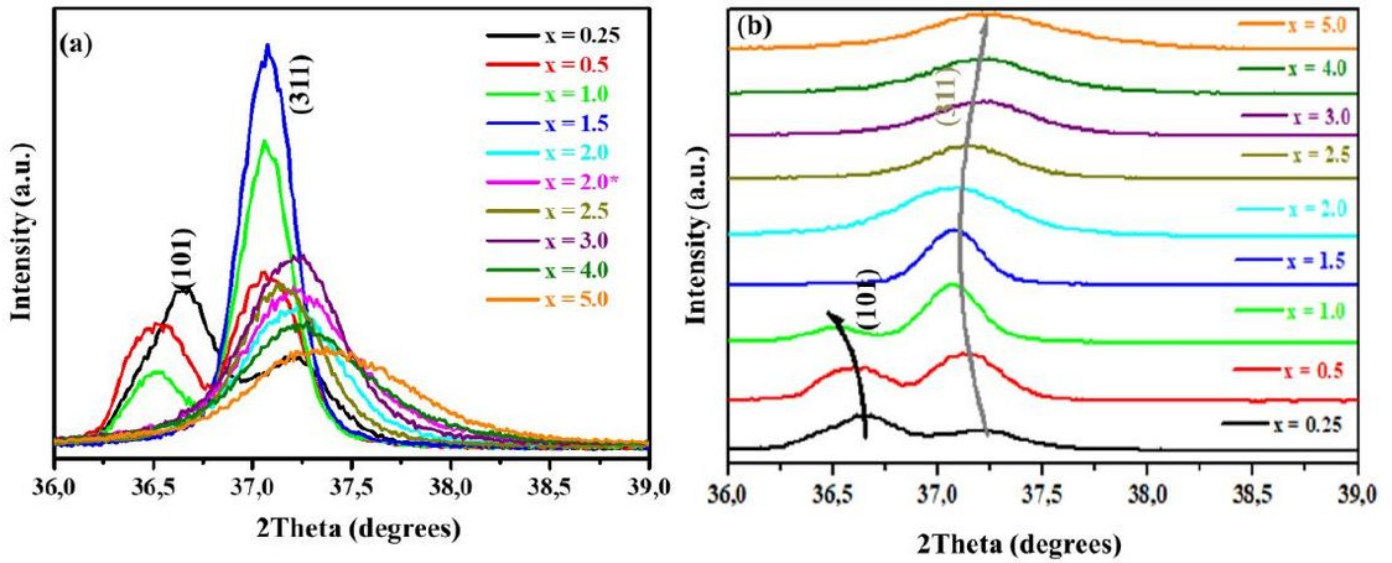


Figure 3

Zoomed analysis of diffraction peak (a) intensity and (b) shift of the (101) ZnO and (311) ZnAl₂O₄ phase of ZnAl_xO_{1.5x + 1} :0.1% Tb³⁺ (0.25 ≤ x ≤ 5.0)

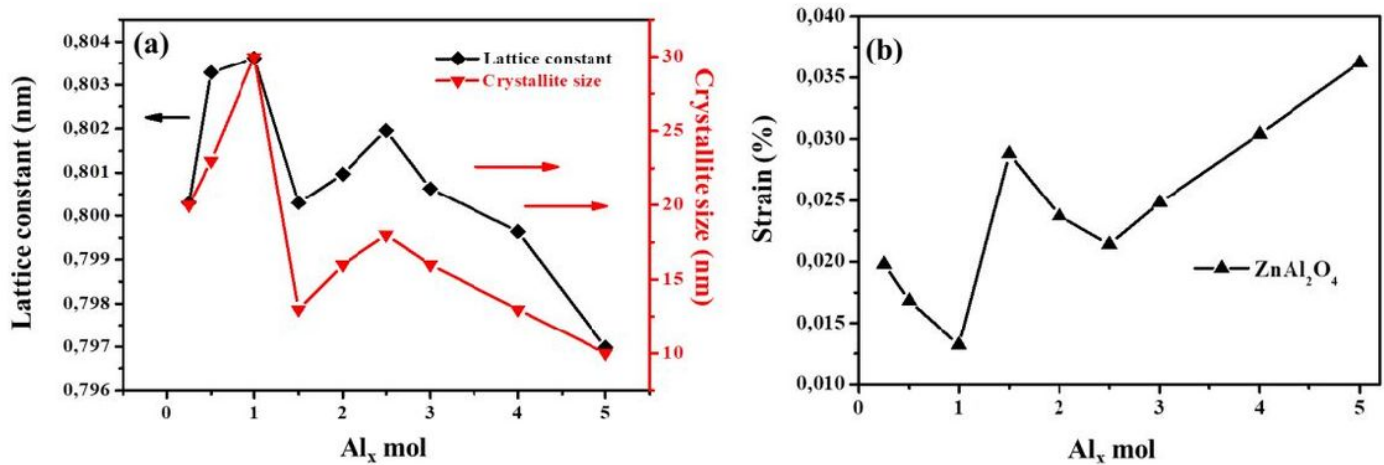


Figure 4

(a) lattice constant and crystallite size (nm); and (b) strain of ZnAl₂O₄ phase as a function of Al_x mol

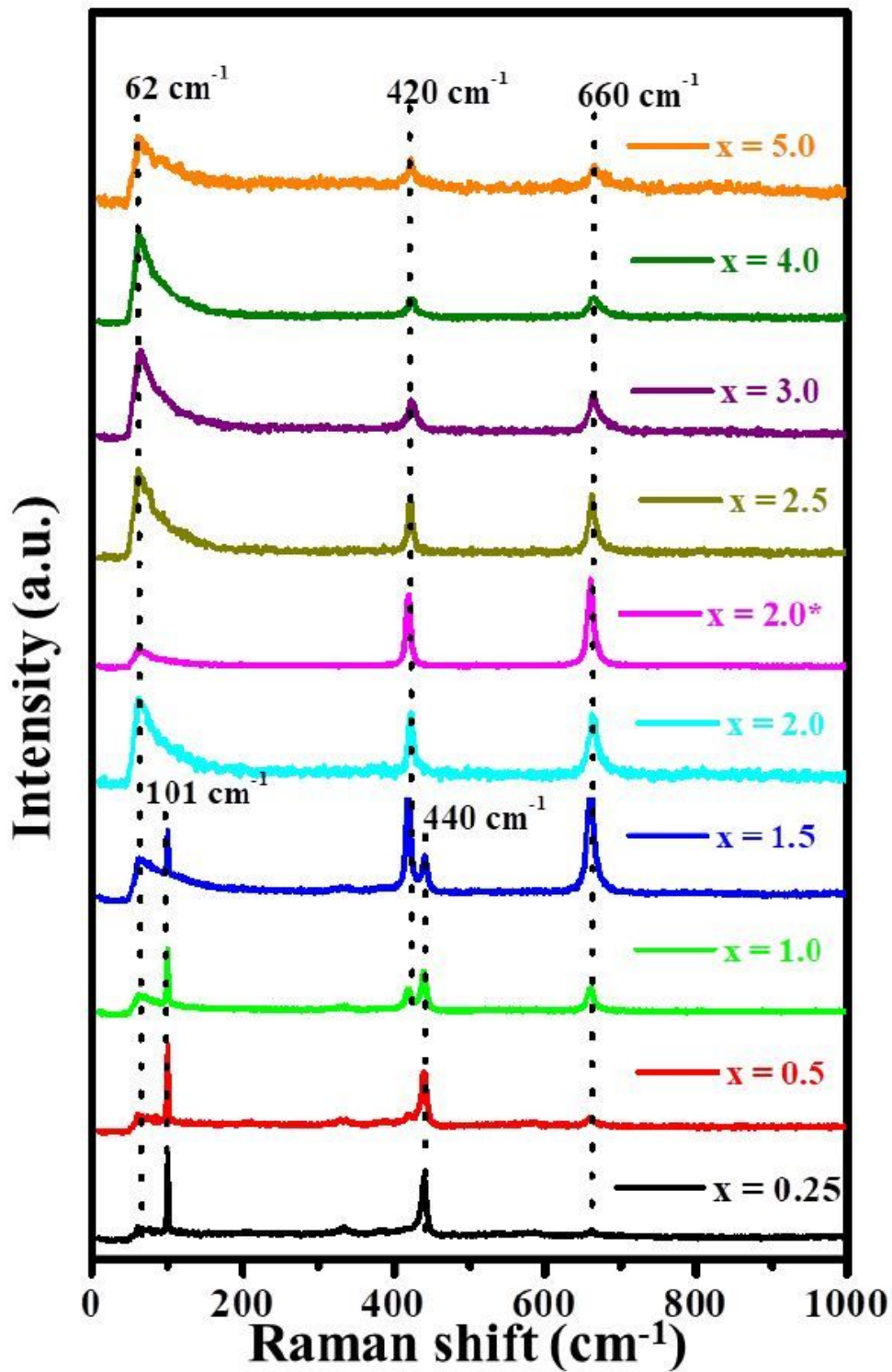


Figure 5

The Spectra for the $x = 2.0^*$ (undoped) and $\text{ZnAl}_x\text{O}_{1.5x+1}:0.1\% \text{ Tb}^{3+}$ ($0.25 \leq x \leq 5.0$)

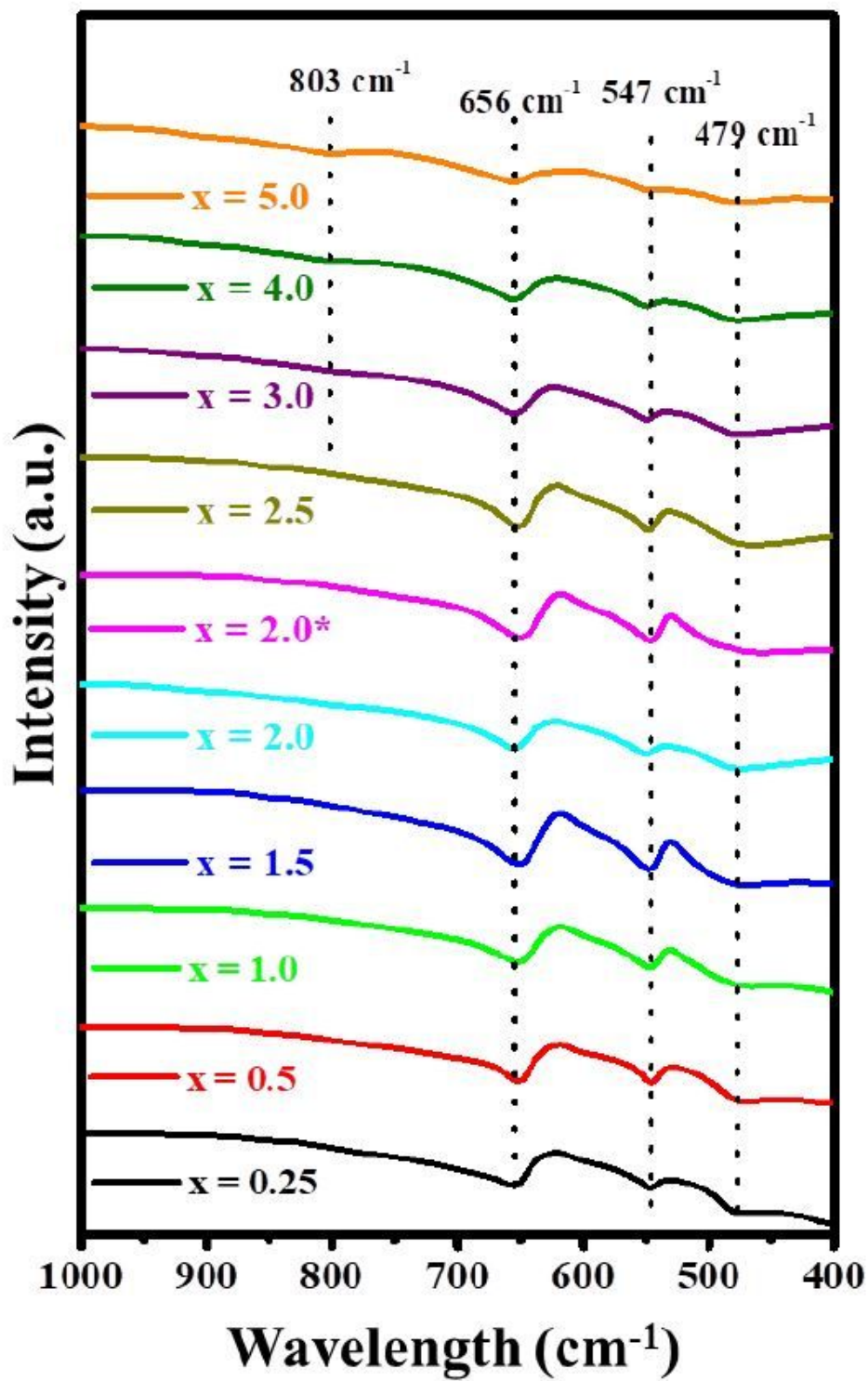


Figure 6

The FTIR spectra for the $x = 2.0^*$ and $\text{ZnAl}_x\text{O}_{1.5x} + 1:0.1\% \text{Tb}^{3+}$ ($0.25 \leq x \leq 5.0$)

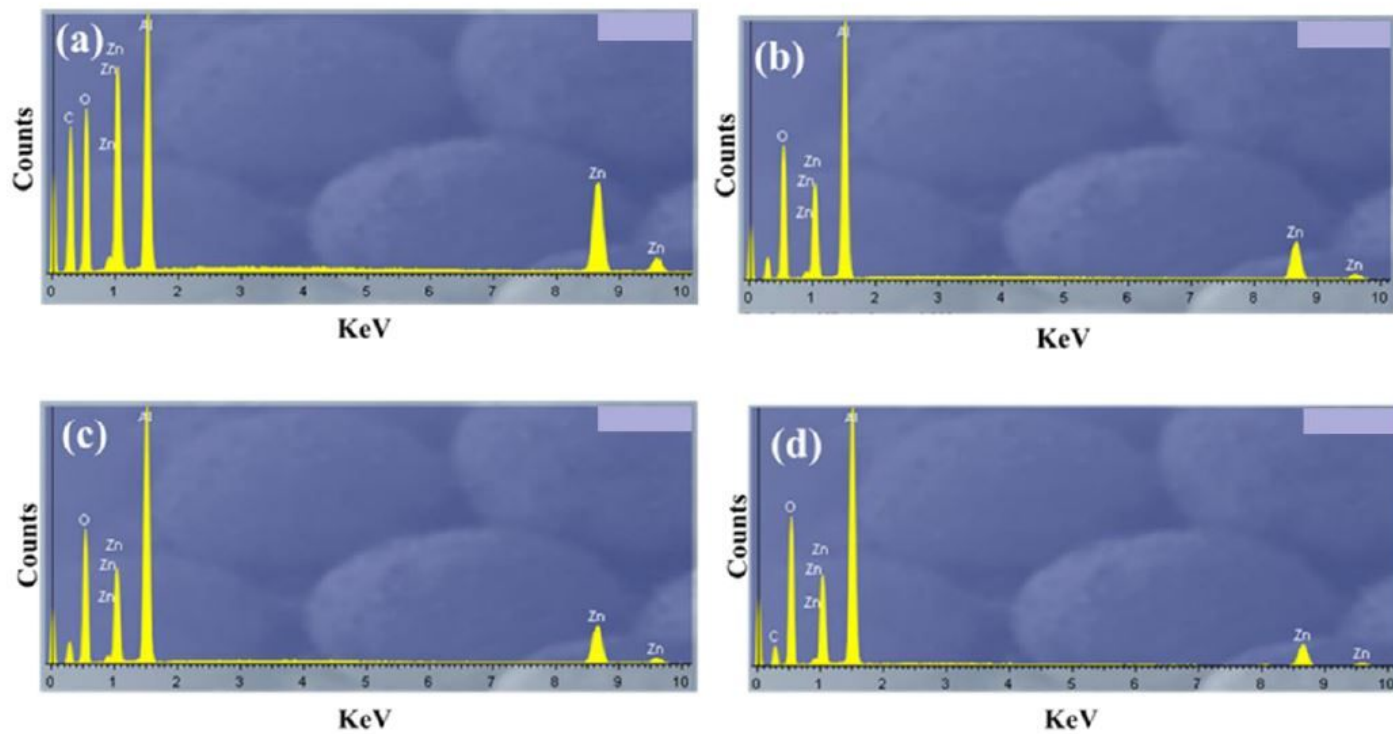


Figure 7

The EDS spectrum of the $\text{ZnAl}_x\text{O}_{1.5x} + 1:0.1\% \text{Tb}^{3+}$ where (a) $x = 0.25$, (b) 2.0^* (un-doped), (c) 2.0 , and (d) 4.0 nano-phosphors

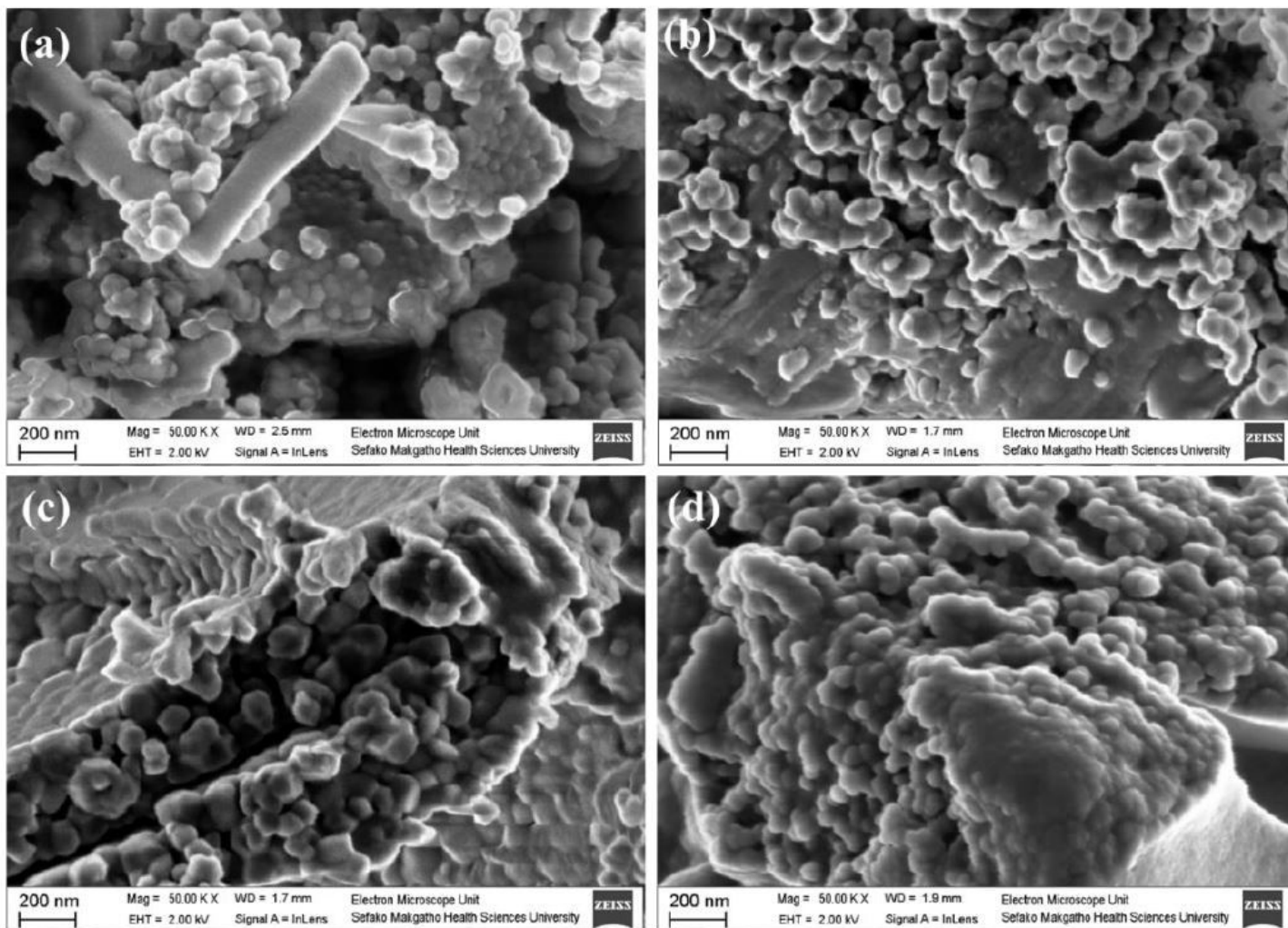


Figure 8

The SEM micrographs of the (a) $x = 0.25$ (b) 2.0^* (un-doped) (c) 2.0, and (d) 4.0 nano-phosphor

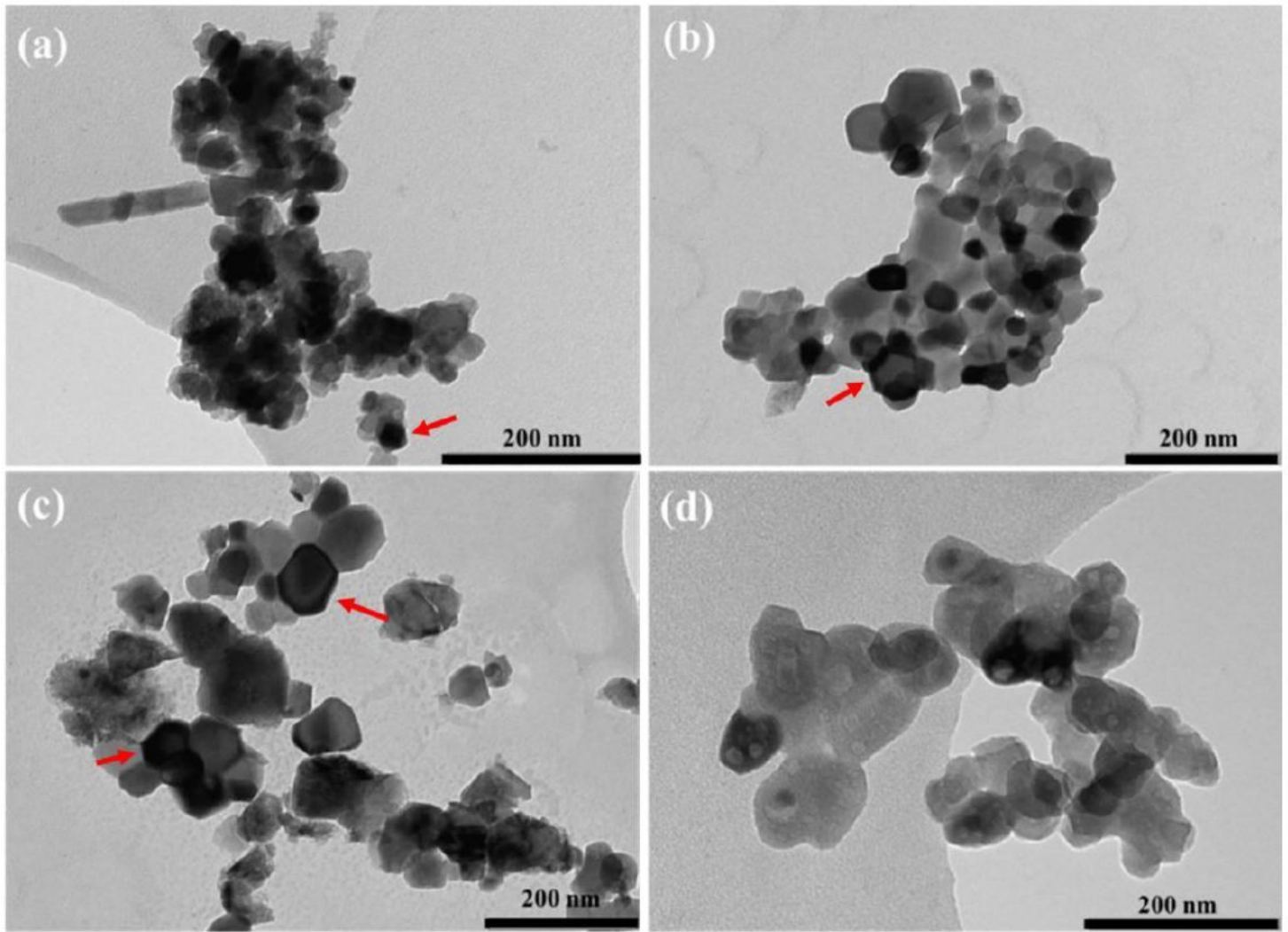


Figure 9

The TEM micrographs of the (a) $x = 0.25$, (b) 2.0^* , (c) 2.0 , and (d) 4.0 nano-phosphor

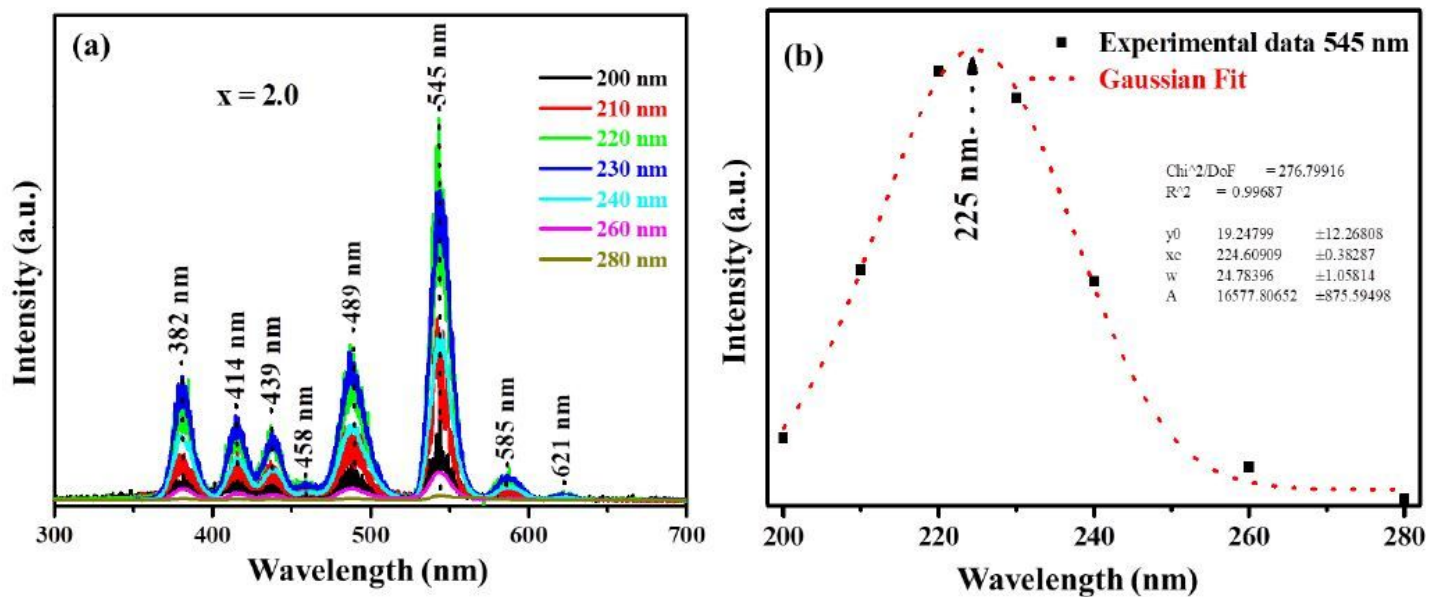


Figure 10

(a) The emission spectra of the $x = 2.0$ sample excited at various excitation wavelength and (b) emission intensity as a function of excitation wavelength

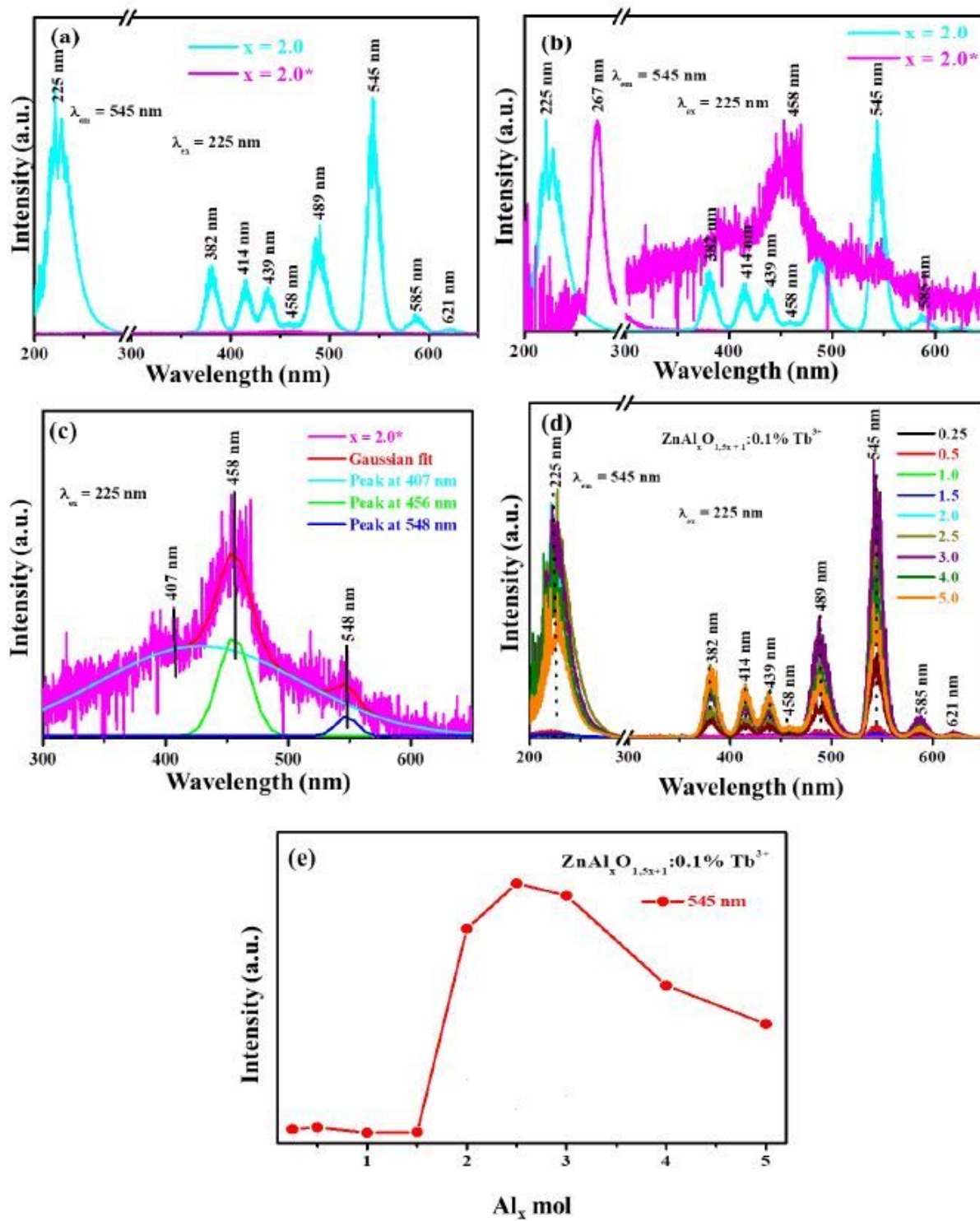


Figure 11

Excitation and emission spectra of the (a) un-doped ($x = 2.0^*$) and doped ($x = 2.0$), (b) normalized of un-doped and doped, (c) deconvolution of the un-doped emission, (d) $\text{ZnAl}_x\text{O}_{1.5x + 1}:0.1\% \text{Tb}^{3+}$ ($0.25 \leq x \leq 5.0$), and (e) emission intensity of the peak located at 545 nm as a function of Alx moles.

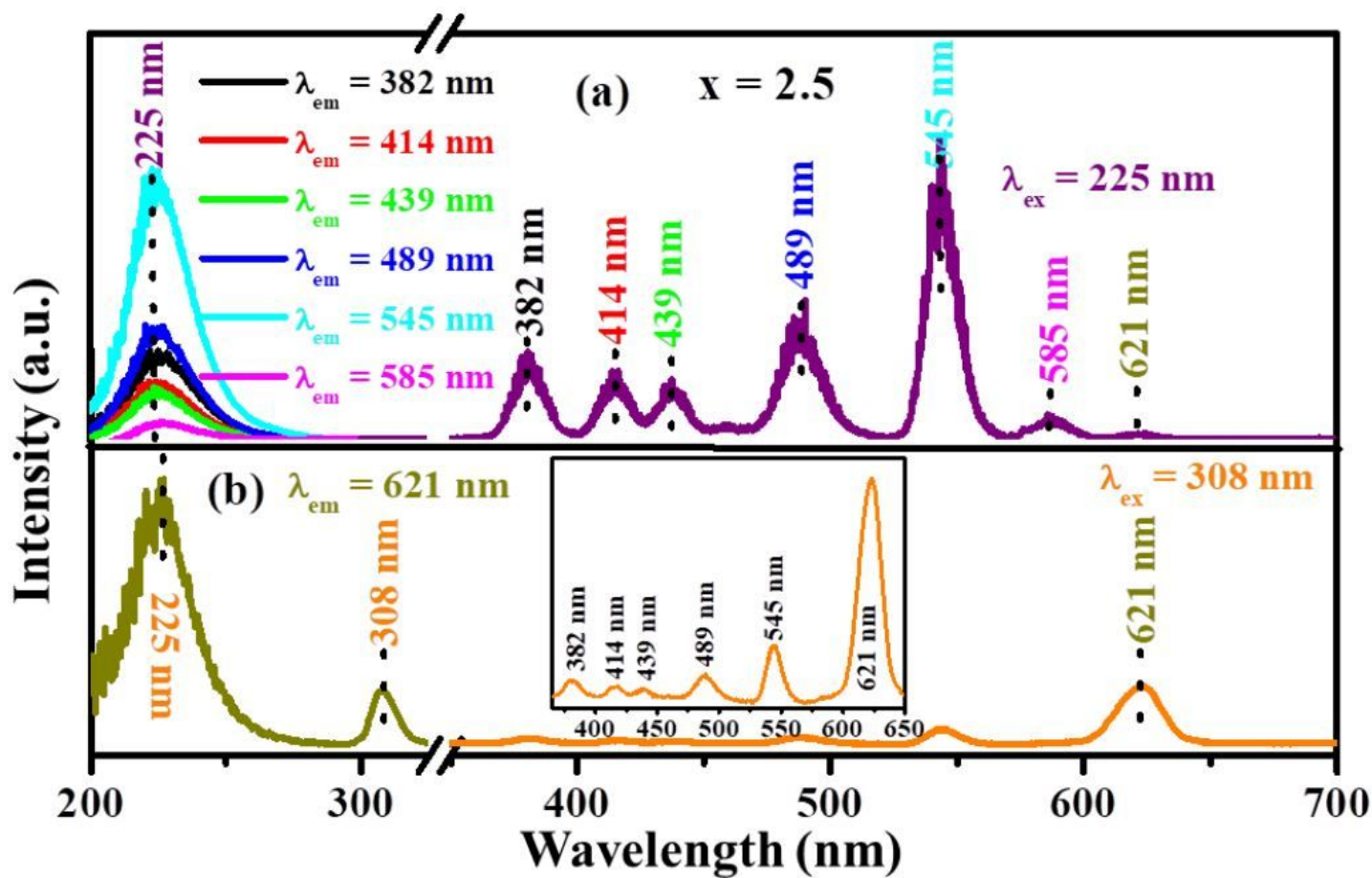


Figure 12

Excitation and emission spectra of the $x = 2.5$ sample

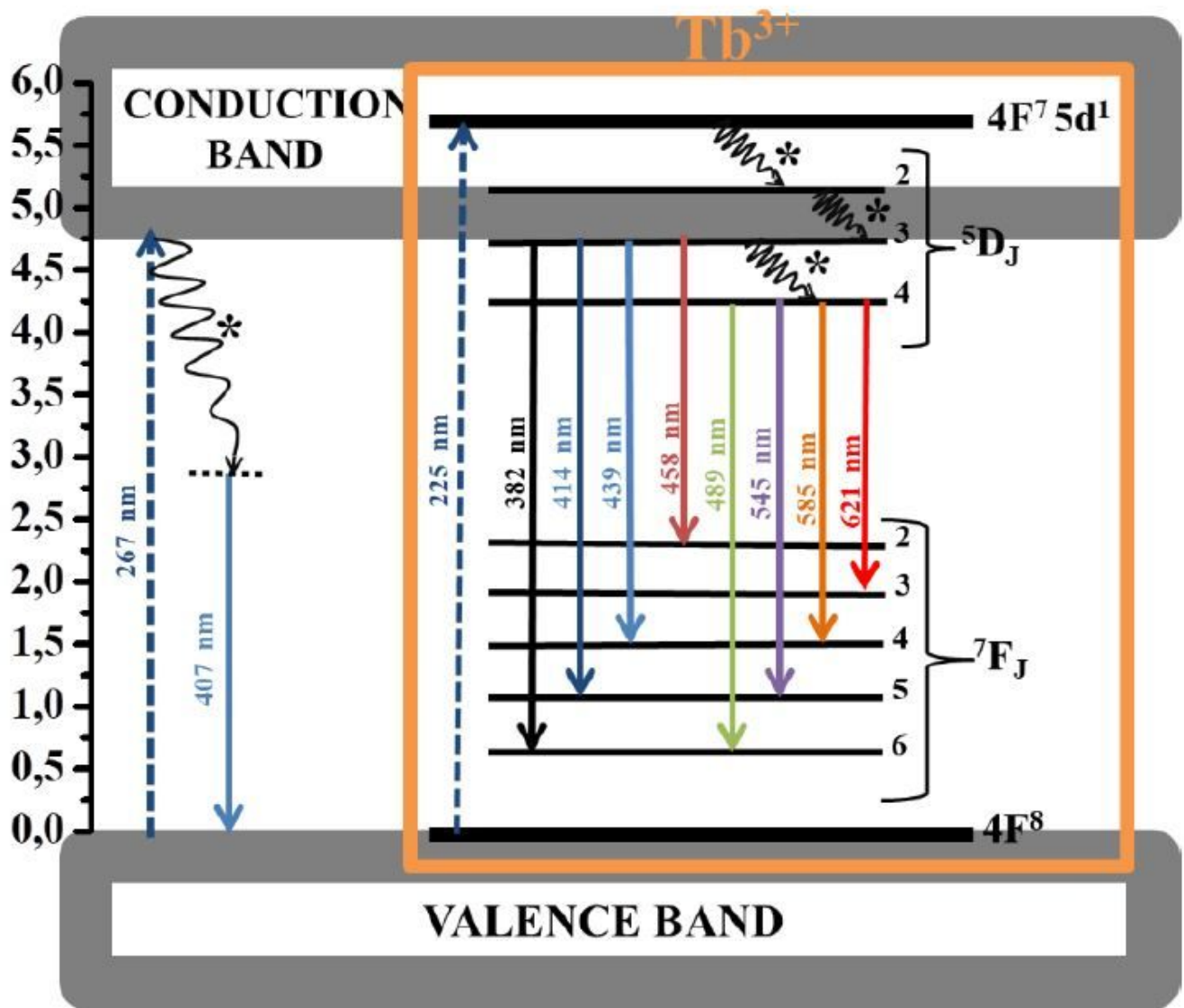


Figure 13

The proposed excitation and emission pathways mechanism for $ZnAl_2O_4:0.1\%Tb^{3+}$ series

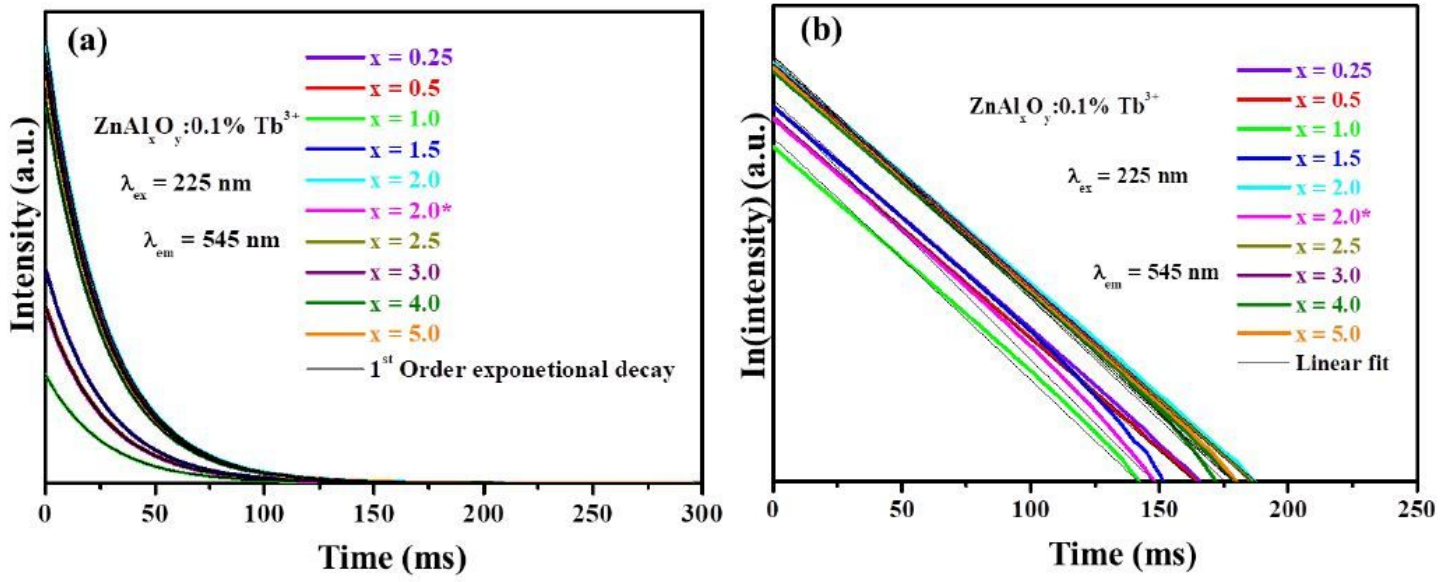


Figure 14

(a) The decay curve and the (b) natural logarithm of the decay curve of host at $x = 2.0$ and ZnAl_xO_y:0.1%Tb³⁺ ($0.25 \leq x \leq 5.0$)

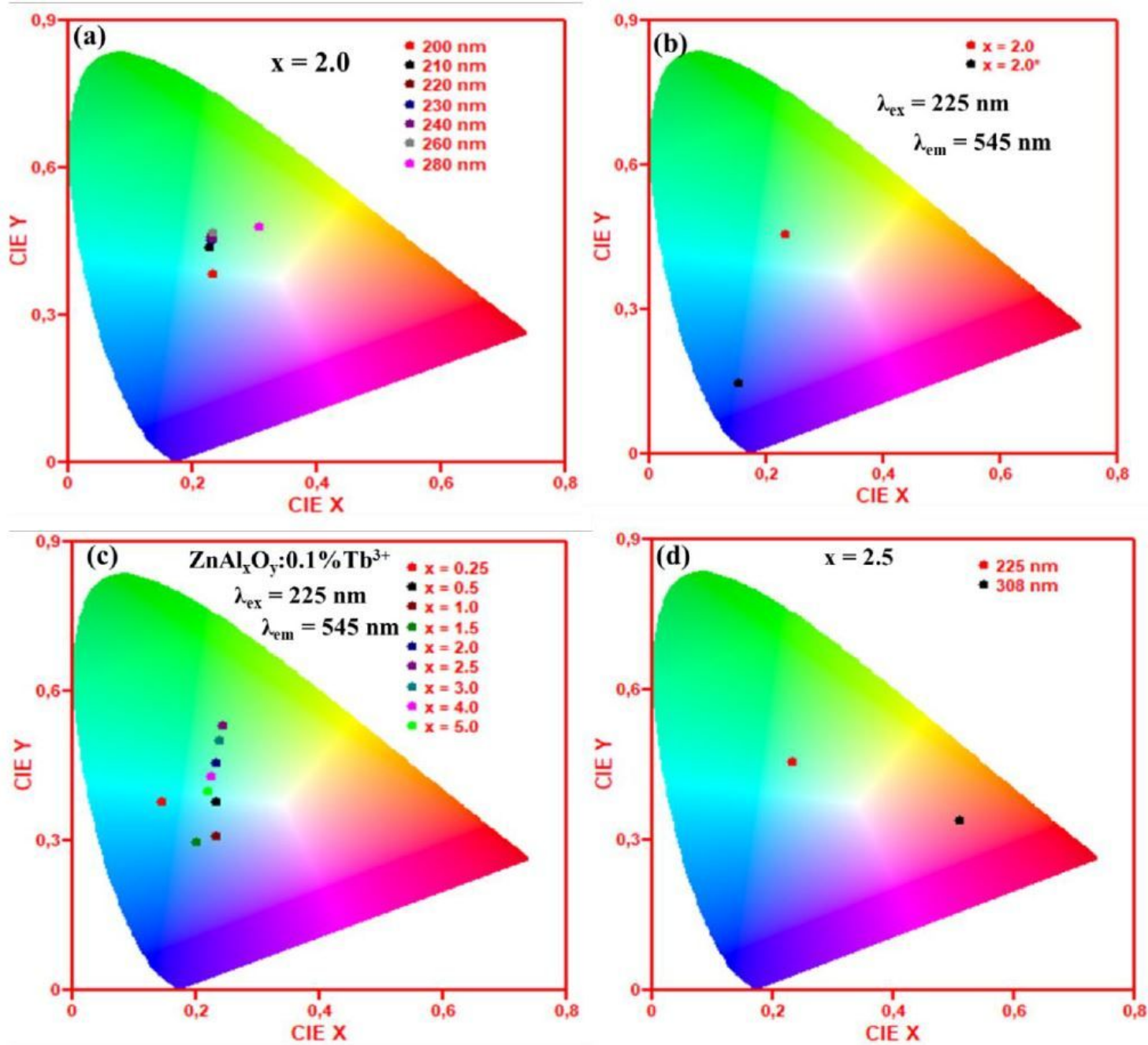


Figure 15

CEI colour for the (a) $x = 2.0$ at various excitation wavelength, (b) Tb³⁺ doped and un-doped sample at $x = 2.0$, (c) ZAOT series, and (d) $x = 2.5$ at the excitation wavelength of 225 and 308 nm